



Publication Year	2017
Acceptance in OA	2020-07-20T15:15:52Z
Title	ATLASGAL-selected massive clumps in the inner Galaxy. III. Dust continuum characterization of an evolutionary sample
Authors	König, C., Urquhart, J. S., Csengeri, T., Leurini, Silvia, Wyrowski, F., GIANNETTI, ANDREA, Wienen, M., Pillai, T., Kauffmann, J., Menten, K. M., Schuller, F.
Publisher's version (DOI)	10.1051/0004-6361/201526841
Handle	http://hdl.handle.net/20.500.12386/26531
Journal	ASTRONOMY & ASTROPHYSICS
Volume	599

ATLASGAL-selected massive clumps in the inner Galaxy

III. Dust continuum characterization of an evolutionary sample*

C. König¹, J. S. Urquhart^{1,2}, T. Csengeri¹, S. Leurini¹, F. Wyrowski¹, A. Giannetti¹, M. Wienen¹, T. Pillai¹, J. Kauffmann¹, K. M. Menten¹, and F. Schuller¹

¹ Max-Planck-Institut für Radioastronomie (MPIfR), Auf dem Hügel 69, 53121 Bonn, Germany
e-mail: koenig@mpifr-bonn.mpg.de

² School of Physical Sciences, University of Kent, Ingram Building, Canterbury, Kent CT2 7NH, UK

Received 26 June 2015 / Accepted 28 October 2016

ABSTRACT

Context. Massive-star formation and the processes involved are still poorly understood. The ATLASGAL survey provides an ideal basis for detailed studies of large numbers of massive-star forming clumps covering the whole range of evolutionary stages. The ATLASGAL Top100 is a sample of clumps selected by their infrared and radio properties to be representative for the whole range of evolutionary stages.

Aims. The ATLASGAL Top100 sources are the focus of a number of detailed follow-up studies that will be presented in a series of papers. In the present work we use the dust continuum emission to constrain the physical properties of this sample and identify trends as a function of source evolution.

Methods. We determine flux densities from mid-infrared to submillimeter wavelength (8–870 μm) images and use these values to fit their spectral energy distributions and determine their dust temperature and flux. Combining these with recent distances from the literature including maser parallax measurements we determine clump masses, luminosities and column densities.

Results. We define four distinct source classes from the available continuum data and arrange these into an evolutionary sequence. This begins with sources found to be dark at 70 μm , followed by 24 μm weak sources with an embedded 70 μm source, continues through mid-infrared bright sources and ends with infrared bright sources associated with radio emission (i.e., H II regions). We find trends for increasing temperature, luminosity, and column density with the proposed evolution sequence, confirming that this sample is representative of different evolutionary stages of massive star formation. Our sources span temperatures from approximately 11 to 41 K, with bolometric luminosities in the range $57 L_\odot$ – $3.8 \times 10^6 L_\odot$. The highest masses reach $4.3 \times 10^4 M_\odot$ and peak column densities up to $1.1 \times 10^{24} \text{ cm}^{-2}$, and therefore have the potential to form the most massive O-type stars. We show that at least 93 sources (85%) of this sample have the ability to form massive stars and that most are gravitationally unstable and hence likely to be collapsing.

Conclusions. The highest column density ATLASGAL sources cover the whole range of evolutionary stages from the youngest to the most evolved high-mass-star forming clumps. Study of these clumps provides a unique starting point for more in-depth research on massive-star formation in four distinct evolutionary stages whose well defined physical parameters afford more detailed studies. As most of the sample is closer than 5 kpc, these sources are also ideal for follow-up observations with high spatial resolution.

Key words. stars: formation – stars: evolution – stars: massive – radiative transfer – surveys

1. Introduction

Massive stars ($>8 M_\odot$) play an important role in the evolution of their host galaxies (Kennicutt 2005). During the early stages of their formation they drive powerful molecular outflows that inject momentum into the surrounding environment. At their later stages they drive strong stellar winds and emit copious amounts of ionizing radiation that shape their local environments and regulate further star formation. Massive stars are also primarily responsible for the production of nearly all heavy elements, which are returned to the interstellar medium (ISM) through stellar winds and supernovae, leading to an enrichment of the local and global environment and changes to the chemistry. Yet the formation and early evolutionary stages of massive star formation are still not well understood (see Zinnecker & Yorke 2007 for a review).

The main hurdles to an improved understanding are that high-mass stars are rare and are therefore typically found at large distances from the Sun (>2 kpc), and that the earliest stages of their formation take place while they are still deeply embedded in their natal molecular clouds. Consequently, the earliest stages are hidden from more traditional observations at optical and near-infrared wavelengths and therefore observations in the far-infrared and submillimeter (submm) regimes are required to probe these extremely dense environments. Furthermore, massive stars are known to form almost exclusively in clusters (de Wit et al. 2004) and therefore high-resolution is required to separate individual (proto-)cluster members.

In recent years, a number of Galactic plane surveys have been undertaken that probe large volumes of the Galaxy and provide a straightforward way to identify a large sample of embedded massive stars and clusters that will include examples of sources in all of the important evolutionary stages. These surveys provide almost complete coverage of near-infrared to radio wavelengths (e.g., the UKIRT Infrared Deep

* Full Table 1, including fluxes, is only available at the CDS via anonymous ftp to cdsarc.u-strasbg.fr (130.79.128.5) or via <http://cdsarc.u-strasbg.fr/viz-bin/qcat?J/A+A/599/A139>

Sky Survey Galactic Plane Survey (UKIDSS GPS), [Lucas et al. 2008](#); Galactic Legacy Infrared Mid-Plane Survey Extraordinaire (GLIMPSE), [Benjamin et al. 2003](#); Midcourse Space Experiment (MSX), [Price et al. 2001](#); Wide-Field Infrared Survey Explorer (WISE) [Wright et al. 2010](#); Multiband Infrared Photometer for *Spitzer* survey of the inner Galactic Plane (MIPS-GAL), [Carey et al. 2009](#); *Herschel* infrared Galactic Plane Survey (Hi-GAL), [Molinari et al. 2010](#); APEX Telescope Large Area Survey of the Galaxy (ATLASGAL), [Schuller et al. 2009](#); Bolocam Galactic Plane Survey (BGPS), [Aguirre et al. 2011](#) and the Co-ordinated Radio and Infrared Survey for High-Mass Star Formation (CORNISH), [Purcell et al. 2013](#) and [Hoare et al. 2012](#)).

Dust emission is generally optically thin at submm wavelengths and therefore surveys at these wavelengths are an excellent tracer of column density and total mass. The ATLASGAL survey covers a total area of 420 square degrees, tracing dust throughout the inner Galaxy ($300^\circ < \ell < 60^\circ$ with $|b| \leq 1.5^\circ$ and was subsequently extended to $-20^\circ < \ell < 300^\circ$ with $-2^\circ < b < 1^\circ$ ([Schuller et al. 2009](#)). The survey was conducted with the Large APEX Bolometer Camera (LABOCA, [Siringo et al. 2009](#)) using the Atacama Pathfinder EXperiment 12 m telescope (APEX; [Güsten et al. 2006](#)), which is located at a height of ~ 5100 m on the Chajnantor plateau in the Atacama desert in Chile. APEX has an angular resolution of $19.2''$ at $870\ \mu\text{m}$.

Subsequently, the ATLASGAL compact source catalog (CSC; [Contreras et al. 2013](#); [Urquhart et al. 2014a](#)) and the ATLASGAL Gaussclumps source catalog (GCSC; [Csengeri et al. 2014](#)) were extracted, identifying $\sim 10\,000$ dust clumps located throughout the inner Galaxy. These catalogs include large numbers of potential high-mass-star forming regions in different evolutionary stages from massive starless regions to clumps associated with (ultra-) compact H II regions on the verge of destroying their natal environment. In the past, studies into massive-star formation have focused on a single well defined evolutionary stage (e.g., UCHII regions, [Wood & Churchwell 1989](#); high-mass protostellar objects, [Sridharan et al. 2002](#); or Class II methanol masers, which exclusively pinpoint the locations of high-mass protostars, [Walsh et al. 1997, 2003](#)). Although many of these have been successful in parameterising these stages they tell us little about how these various phases are connected, how their properties change as the embedded star evolves or the relative lifetimes of each stage. However, covering the full mid-infrared to submm wavelength regime with unprecedented sensitivity and resolution, the above-mentioned unbiased Galactic plane surveys and in particular the ATLASGAL catalogs provide an excellent starting point to study the complete evolutionary sequence of massive stars in a robust statistical manner ([Urquhart et al. 2014a](#)).

We have used the ATLASGAL survey to select a sample of ~ 100 massive clumps that likely represent different evolutionary stages ([Giannetti et al. 2014](#)). We have also correlated this sample with methanol masers ([Urquhart et al. 2013a](#)), young stellar objects (YSOs) and H II regions ([Urquhart et al. 2013b, 2014b](#)) to constrain the evolutionary state of the sample's sources. This sample has also been the subject of molecular line follow-up studies to fully characterize the evolutionary sequence and derive the physical properties of different stages. The results of these studies have been discussed in a series of papers. For example, CO depletion and isotopic ratios have been investigated by [Giannetti et al. \(2014\)](#), SiO emission for the northern sources to trace shocked gas was studied by [Csengeri et al. \(2016\)](#), and NH₃ has been used to investigate infall towards selected sources

by [Wyrowski et al. \(2016\)](#) with a number of papers in preparation focusing on their associated outflows (Navarrete et al., in prep.) and modeling of their chemistry (Giannetti et al., in prep.). Using these spectroscopic and continuum surveys will provide the most detailed view of the evolutionary sequence of massive stars and robust constraints on the physical properties, chemical conditions, and kinematics of this unique sample of high-mass-star forming regions selected from the whole inner Galactic plane.

In this paper we use multi-wavelength dust continuum emission to characterize this sample of candidate massive-star forming regions, in terms of dust temperatures, bolometric luminosities, and clump masses. Together with the latest distances, these quantities are key to the further analysis of the sample. To derive the sources' physical properties from dust continuum spectral energy distributions (SEDs), we complement the $870\ \mu\text{m}$ ATLASGAL data with publicly available *Herschel*/Hi-GAL ([Molinari et al. 2010](#)), MSX ([Egan et al. 2003](#)), and WISE ([Wright et al. 2010](#)) data in order to cover a wavelength range from $8\ \mu\text{m}$ to $870\ \mu\text{m}$. Furthermore, we show that our sample comprises a representative set of sources covering all of the important embedded evolutionary stages of massive-star formation.

This paper is organized as follows: in Sect. 2 we describe how the initial selection was made and briefly discuss how the source classification has evolved as new survey data have become available. In Sect. 3 we explain how the photometry and SEDs have been obtained. In Sect. 4 we derive physical parameters from the results of the SED modeling, while in Sect. 5 we discuss the assignment of our sources to different stages of development and an evolutionary sequence. In Sect. 6 we summarize our findings and present a brief outlook on future work.

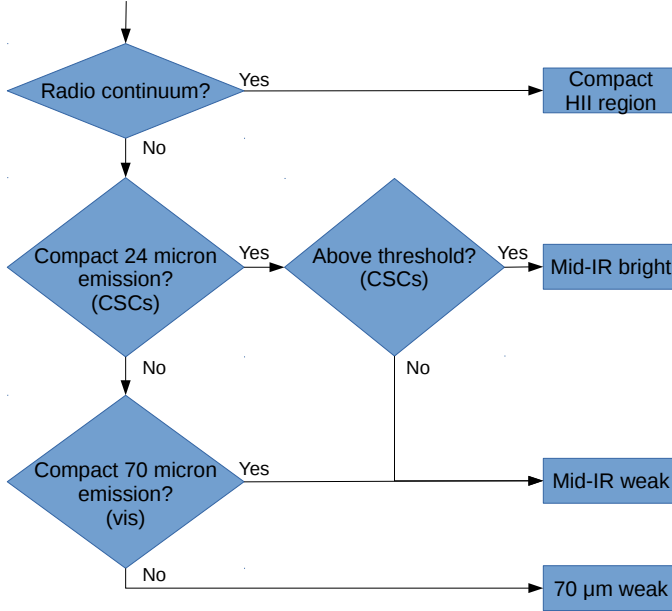
2. Sample selection and classification

We selected 110 sources from the ATLASGAL compact source catalog that are likely to be at different evolutionary stages, using ancillary data to trace their star formation activity. We originally selected 102 sources as being the brightest sources at submm wavelengths in four distinct groups as described by [Giannetti et al. \(2014\)](#), using ancillary mid-infrared and radio data. During various ongoing follow-up projects, eight sources were added, and here we investigate the physical properties of this sample of 110 sources as a necessary reference for future studies. In the following sections we refer to this sample as the ATLASGAL “Top100”.

2.1. Classification

Since the initial classification of the sources by [Giannetti et al. \(2014\)](#), new catalogs have become available, allowing for a refined classification that better reflects the physical properties of the sources in different evolutionary stages. In this paper, we re-classify our sample using four distinct phases of massive-star formation. Three of these phases are drawn from the scheme originally outlined by [Giannetti et al. \(2014\)](#) and [Csengeri et al. \(2016\)](#); i.e., mid-infrared weak, mid-infrared bright and HII regions). Here we refine this classification and extend it to include the youngest starless/pre-stellar phase based on the physical properties of the sample.

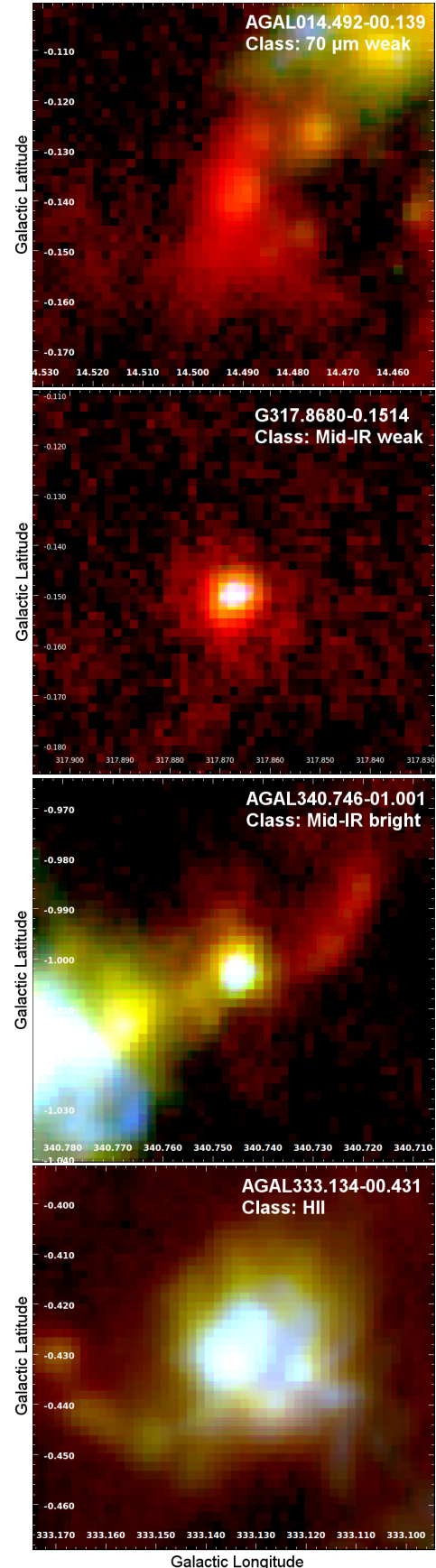
A schematic diagram of the classification process is shown in Fig. 1. First, the sources are checked for radio continuum emission using the CORNISH survey ([Hoare et al. 2012](#); [Purcell et al. 2013](#)), the RMS survey ([Urquhart et al. 2007, 2009](#)), or the targeted observations towards methanol masers

**Fig. 1.** Classification process for the Top100 sample.

reported by [Walsh et al. \(1998\)](#). When radio continuum emission is found at either 4 or 8 GHz within $10''$ of the ATLASGAL peak, the source is considered to be a compact H II region. We have adopted the radius of $10''$ as our association criterion from [Urquhart et al. \(2014c\)](#), where they compared the angular offsets between the peak of the submm emission and a number of massive-star formation tracers, determining that ~ 85 per cent of compact embedded objects were located within $10''$ of each other. Furthermore, we refined the distinction between mid-infrared weak and mid-infrared bright sources by inspecting the emission in the $21\ \mu\text{m}$ MSX ([Price et al. 2001](#)) and $24\ \mu\text{m}$ MIPSGAL ([Carey et al. 2009](#)) images. Looking for signs of star-formation, a source is considered mid-infrared bright if there is a compact mid-infrared source associated with the submm emission peak and the flux reported in the compact source catalogs ([Egan et al. 2003](#); [Gutermuth & Heyer 2015](#)) is above $2.6\ \text{Jy}$, corresponding to a 4, 8, or $15\ M_{\odot}$ star at 1, 4, and $20\ \text{kpc}$, respectively ([Heyer et al. 2016](#)). Accordingly a source is considered to be mid-infrared weak when the compact mid-infrared emission in the $21/24\ \mu\text{m}$ band is below $2.6\ \text{Jy}$ or no compact source is associated with the peak. Finally, the sources in the starless/pre-stellar phase are identified from a visual inspection of Hi-GAL PACS $70\ \mu\text{m}$ images. Showing no compact emission at $70\ \mu\text{m}$ within $10''$ of the submm emission peak, a source is considered $70\ \mu\text{m}$ weak. This means that sources showing diffuse emission at $70\ \mu\text{m}$ or compact $70\ \mu\text{m}$ sources offset from the dust peak are still considered as $70\ \mu\text{m}$ weak clumps.

In Fig. 2 we show example three color images for each class and below we briefly describe the observed features of each phase and give the number of sources classified in each:

- Starless/pre-stellar stage (16 sources): a quiescent phase, which represents the earliest stage of massive-star formation (Fig. 2, top panel). These clumps are either mostly devoid of any embedded pointlike sources in the Hi-GAL $70\ \mu\text{m}$ images or only show weak emission. They are likely to be the coldest and least luminous sources of the whole sample, and may already be collapsing, but no protostellar object has yet formed (e.g., [Motte et al. 2010](#); [Elia et al. 2013](#); [Traficante et al. 2015](#)). This class is called “ $70\ \mu\text{m}$ weak” from here on.

**Fig. 2.** Three-color images of sample sources for each class sorted from youngest (top) to most evolved (bottom). Size: $5' \times 5'$; red: ATLASGAL $870\ \mu\text{m}$; green: PACS $160\ \mu\text{m}$; blue: PACS $70\ \mu\text{m}$.

- Protostellar stage (33 sources): compact point sources are clearly seen in the $70\ \mu\text{m}$ Hi-GAL image and so protostellar objects are present (Fig. 2, second panel). The embedded $70\ \mu\text{m}$ sources are either not associated with any mid-infrared counterparts within $10''$ of the peak emission or the associated compact emission is below our threshold of $2.6\ \text{Jy}$, which indicates that the star formation is at an early stage and that the clumps are likely to be dominated by cold gas. We call this class “mid-IR weak” throughout the paper.
- High-mass protostellar stage (36 sources): this phase is characterized by strong compact mid-infrared emission seen in 8 and 24 micron images and is one of the most active stages of massive-star formation (Fig. 2, third panel). These clumps are likely undergoing collapse in the absence of a strong magnetic field (Urquhart et al. 2014c, 2015), show signs of infall (Wyrowski et al. 2016) and are likely to be driving strong outflows (Navarete et al., in prep.). Due to the infall, outflows, and already active young stellar objects, these sources are also likely to be significantly hotter than the sources in the quiescent phase, giving rise to the bright emission at mid-IR wavelengths (called “mid-IR bright” from here on).
- Compact H II region phase (25 sources): in the latest evolutionary phase of massive-star formation we define here, the sources have just begun to disperse their natal envelope and are ionizing their local environment, creating compact H II regions (Fig. 2, bottom panel). These sources are associated with bright mid-infrared emission and compact radio continuum emission arising from the ionization of their environment, making them easily distinguishable from the earlier evolutionary phases. We refer to this class as “HII regions” from here on.

2.2. Distances

We have determined distances for 109 of the 110 sources of the sample. These distances have been drawn from the literature and supplemented with our own kinematic distances (Wienen et al. 2015). The distances given in Table 1 are based on those given by Giannetti et al. (2014) but incorporate the results of the latest maser parallax measurements reported by Reid et al. (2014); this has resulted in the distances for six sources changing by $\sim 2\ \text{kpc}$. For a small number of sources the distances adopted by Giannetti et al. (2014) disagreed with distances reported in the literature. Given that the distances extracted from the literature are kinematic in nature and have been determined using the same HI data and comparable radial velocity measurements these variations likely result from slight differences in the method applied and the sensitivity and transition of the line surveys used in different studies.

There are eight sources where the literature distance and distance adopted by Giannetti et al. (2014) disagree by more than a few kpc. For one source (AGAL330.954–00.182¹) higher resolution HI data have become available from targeted follow-up observations made toward UC H II regions (Urquhart et al. 2012) and we have adopted the distance obtained from the analysis of this data, which utilizes the presence or non-presence of HI self absorption as a distance indicator. We have examined the mid-infrared images for the other seven sources and find three to be coincident with localized areas of extinction, which would suggest that a near distance

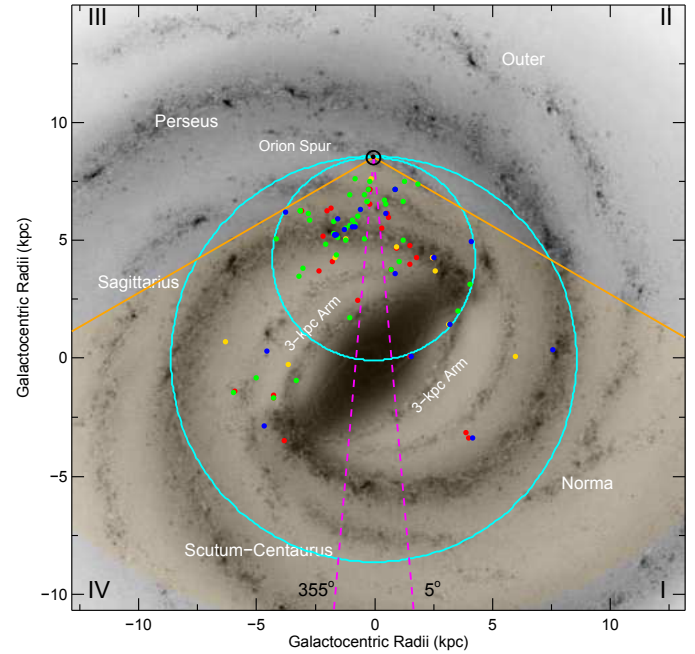


Fig. 3. Galactic distribution of the ATLASGAL Top100 sample. The positions of the H II regions, mid-infrared bright, mid-infrared weak and $70\ \mu\text{m}$ weak sources are indicated by the blue, green, red, and yellow filled circles, respectively. The orange shaded area indicates the region of the Galactic plane covered by the ATLASGAL survey to a distance of $20\ \text{kpc}$, within which the survey is complete for compact clumps with masses $>1000\ M_{\odot}$. The background image is a schematic of the Galactic disc as viewed from the Northern Galactic Pole (courtesy of NASA/JPL-Caltech/R. Hurt (SSC/Caltech)). The Sun is located at the apex of the wedge and is indicated by the \odot symbol. The smaller of the two cyan dot-dashed circles represents the locus of tangent points, while the larger circle traces the solar circle. The spiral arms are labeled in white and Galactic quadrants are given by the roman numerals in the corners of the image. The magenta line shows the innermost region toward the Galactic center where distances are not reliable.

is more likely (AGAL008.684–00.367, AGAL008.706–00.414, and AGAL353.066+00.452). Examination of the HI data towards AGAL316.641–00.087 reveals absorption at the source velocity and so we place this source at the near distance. The lack of an absorption feature in the HI data or evidence of extinction would suggest that the three remaining sources are located at the far distance and indeed for three sources this is likely to be the case (AGAL337.704–00.054, AGAL337.176–00.032, and AGAL337.258–00.101; Giannetti et al. 2015). For one source (AGAL008.831–00.027) we did not obtain a distance, as its radial velocity is close to zero ($V_{\text{LSR}} = 0.53\ \text{km s}^{-1}$), hence rendering a kinematic distance unreliable.

In Fig. 3 we present the distribution of the Top100 on a schematic diagram of the Milky Way that includes many of the key elements of Galactic structure, such as the location of the spiral arms and the Galactic long and short bars (Churchwell et al. 2009).

In Fig. 4 we show the distance distribution of the Top100 sources, which features two distinct peaks at $\sim 2\ \text{kpc}$ and $\sim 4\ \text{kpc}$. These peaks correlate with the near parts of the Sagittarius and Scutum-Centaurus arms, respectively, as seen in Fig. 3. We note that we only show the histogram for the full sample, as the sources in all four phases have a similar distance distribution.

¹ We use source names from Contreras et al. (2013).

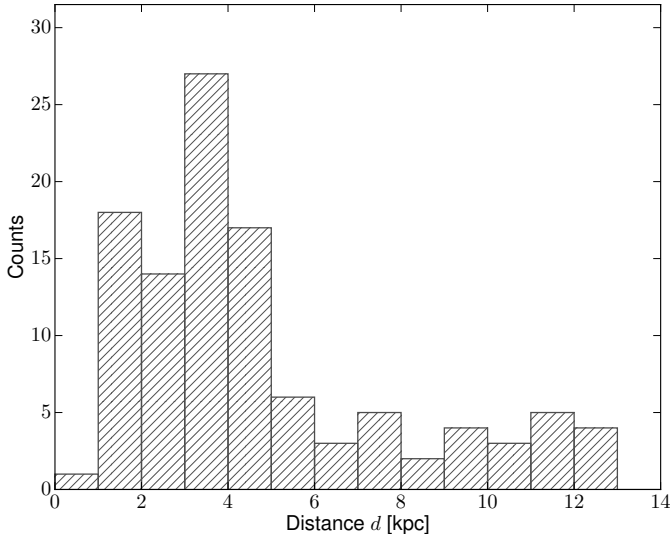


Fig. 4. Heliocentric distance distribution of all ATLASGAL Top100 sources for which a distance has been unambiguously determined. The bin size is 1 kpc.

This is confirmed by Anderson-Darling tests² (Stephens 1974) performed for the different classes yielding p -values higher than 0.02 for all classes, confirming the null hypothesis of two samples being drawn from the same distribution at the 3σ significance level. Furthermore, there is a drop-off in the number of sources beyond a distance of 6 kpc. As the whole sample is selected so that the brightest sources in the ATLASGAL catalog were selected for each category, a general distance bias toward closer distances and being located in the closest spiral arms is not surprising.

3. Spectral energy distributions

The evolutionary scheme for high-mass star formation described in Sect. 2 is primarily based on the visual examination of infrared images and the presence or absence of an infrared embedded point source and is therefore largely a phenomenological classification scheme. To robustly test this evolutionary sequence we need to determine the sample members' physical properties and search for trends in these parameters that support this. Key elements are the source temperatures and bolometric luminosities, which can be determined from model fits to the source's SEDs.

To achieve this goal we extracted multi-wavelength continuum data (mid-infrared to submm wavelengths) and performed aperture photometry to reconstruct the dust continuum SEDs. The fluxes obtained from the photometry were fitted with a simple model to derive the dust temperature and integrated flux, which were subsequently used to estimate the bolometric luminosities and total masses. The data used and methods supplied will be described in detail in the following subsections.

3.1. Dust continuum surveys

The mid-infrared wavelength regime is covered using archival data from either the MSX (Egan et al. 2003) or the WISE

(Wright et al. 2010) surveys. The far-infrared spectrum is covered by the two *Herschel* (Pilbratt et al. 2010) instruments SPIRE (Griffin et al. 2010) and PACS (Poglitsch et al. 2010), covering the wavelength range from $70 \mu\text{m}$ up to $500 \mu\text{m}$, with five different bands centered at 70 , 160 , 250 , 350 , and $500 \mu\text{m}$, respectively. These bands are especially well suited to determine the peak of the SED for cool dust. The level 2.5 maps from the *Herschel* Infrared Galactic Plane Survey (Hi-GAL, Molinari et al. 2010) were retrieved from the *Herschel* Science Archive (HSA)³, and were downloaded in version 11 of the Standard Product Generation (SPGv11) pipeline. To obtain the flux for the longest wavelength (submm) entry of the SED, the $870 \mu\text{m}$ ATLASGAL maps are used.

For all of these data sets we extracted 5×5 arcminute-sized images centered on the source positions. Where necessary the map units were converted to Jy pixel^{-1} while keeping the original resolution. For MSX and WISE images this meant converting from $\text{W m}^{-2} \text{sr}^{-1}$ and digital numbers (DN) to Jy pixel^{-1} , respectively⁴.

3.2. Aperture photometry

Aperture photometry was used to extract fluxes in a consistent way from the mid-infrared and submm maps. The flux density F_{aper} was integrated over a circular aperture centered on the peak flux pixel position. The peak position was identified in either the $250 \mu\text{m}$, $160 \mu\text{m}$ or the $870 \mu\text{m}$ band, depending on whether the band was suffering from saturation, following the order of the bands as previously stated. Assuming a Gaussian-shaped source brightness profile with a full width at half maximum size (FWHM) as reported in Csengeri et al. (2014), we use an aperture size for each source with a radius of 3σ , where $\sigma = \text{FWHM}/(2\sqrt{2\ln 2})$ to obtain most of the flux ($>99\%$) of a source. With a minimum aperture size of $55.1''$ the apertures were also selected such that they are resolved by the lowest resolution data (i.e. $36.6''$ for SPIRE $500 \mu\text{m}$). We performed tests that revealed that smaller aperture sizes underestimate the flux, while a larger aperture size might cut into some other emission nearby, as the source confusion for some of the clumps of our sample is significant, since these are associated with some of the most active star-forming sites in the Galaxy. Subsequently, the background flux density F_{bg} obtained from the median pixel value of a circular annulus around the same center position as the aperture was subtracted from the aperture flux to obtain the background-corrected source flux F .

When fluxes could be successfully extracted from the MSX maps, we preferred these over the WISE fluxes, as the MSX maps have a resolution of $18''$ similar to the longer wavelength bands (e.g., $19.2''$ for ATLASGAL). In addition, MSX suffers less from saturation than the WISE data (compare, e.g., Cutri et al. 2012, Chap. VI.3; and Robitaille et al. 2007, Table 1). In cases where the photometry extracted from the MSX images is a non-detection we turned to the higher sensitivity WISE data to determine the flux.

An example for the photometry extraction in the far-infrared to submm bands is presented in Fig. 5, showing the position and size of the aperture and annulus used to estimate the background

³ http://hereschel.esac.esa.int/Science_Archive.shtml

⁴ For more information see <http://irsa.ipac.caltech.edu/applications/MSX/MSX/imageDescriptions.htm> and http://wise2.ipac.caltech.edu/docs/release/prelim/expup/sec2_3f.html#tbl1

² We chose the Anderson-Darling test over a Kolmogorov-Smirnov test, as it is more sensitive to subtle differences in smaller samples (compare, e.g., Razali & Wah 2011).

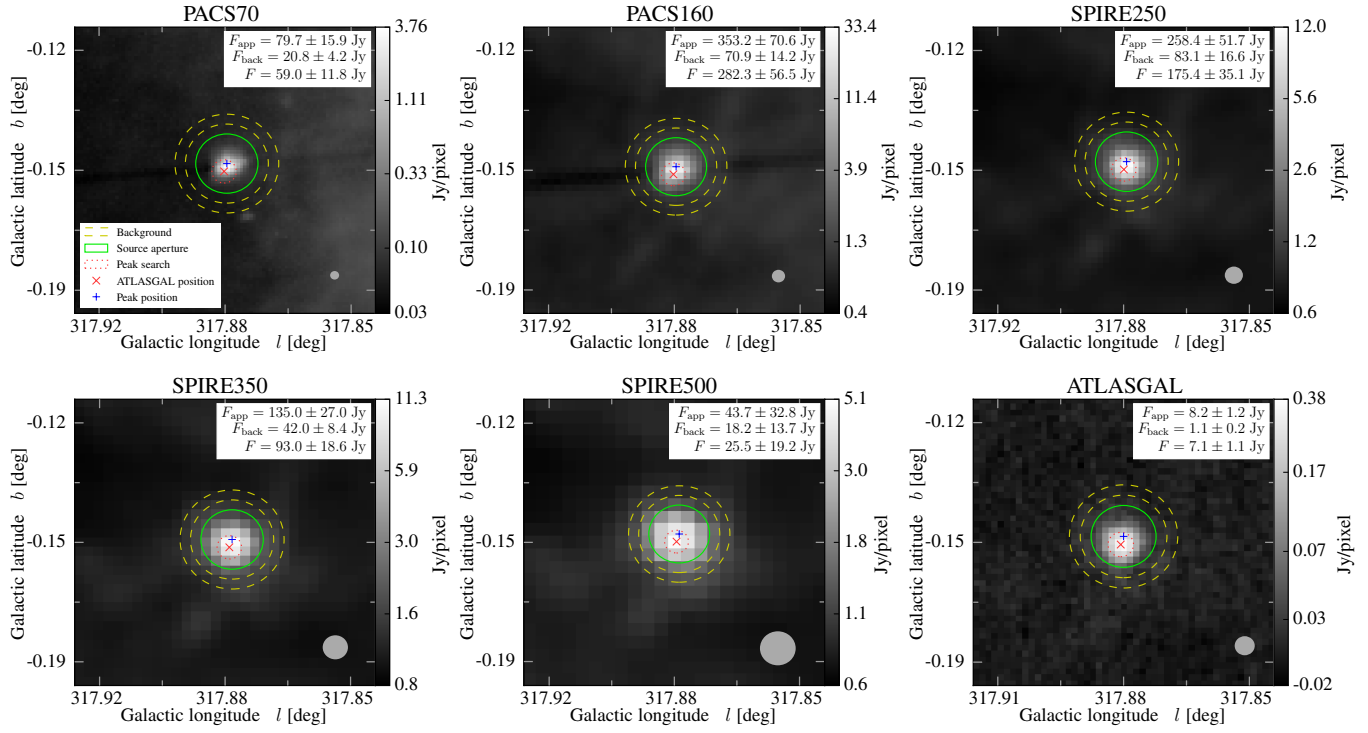


Fig. 5. Images of a single source (AGAL317.867–00.151) seen in the different bands, showing the aperture (green circle), background annulus (yellow dashed circle), ATLASGAL and peak flux position (red and blue crosses, respectively) and the peak pixel search area (red dotted circle). The beam size is indicated as a gray circle in the lower right corner.

contribution for this source. In total, we found one source to be saturated at $70\ \mu\text{m}$, one source at $160\ \mu\text{m}$, 39 sources are saturated at $250\ \mu\text{m}$ and 14 sources at $350\ \mu\text{m}$. When one or more bands in the far-infrared to submm range suffers from saturation, the SPIRE $250\ \mu\text{m}$ band is always one of them. Moreover we note that the fraction of sources being saturated in at least one band increases through the classes: from no source suffering from saturation for the $70\ \mu\text{m}$ weak sample, six sources (i.e., 16%) of the mid-infrared weak class, ten in the mid-infrared bright sample (i.e., 31%), and 23 (i.e., 92%) for the HII regions. For the photometry, the saturated pixels were set to the maximum pixel value of the image, and the flux is only taken as a lower limit for the SED fitting (see Sect. 3.3). To ensure good fitting results we require at least three bands in the far-IR to submm regime to be free from saturation.

In Fig. 6 we show the emission profiles of the submm bands for a single source (AGAL317.867–00.151). To better emphasize the structure and make it comparable between the different bands, for each wavelength we subtracted the median background emission as determined far away (i.e., five times the aperture size) from the source where the profile gets flat and then normalized the flux to the peak emission in that band. As can be seen from the plot, the SPIRE $500\ \mu\text{m}$ band traces the more extended emission, falling off to the background plateau level rather slowly compared to the other bands. Conversely, the other bands trace the peak of the emission within the aperture, but the background aperture still cuts into some local plateau associated with the cloud. The contribution of this is lower than 10% for all bands except the SPIRE $500\ \mu\text{m}$. Accordingly we assume a rather large measurement uncertainty of 50% for the $500\ \mu\text{m}$ band to account for the added uncertainty from the background correction as well as to account for the large pixel size of $15''$ in this band. For the other *Herschel* bands we assume a

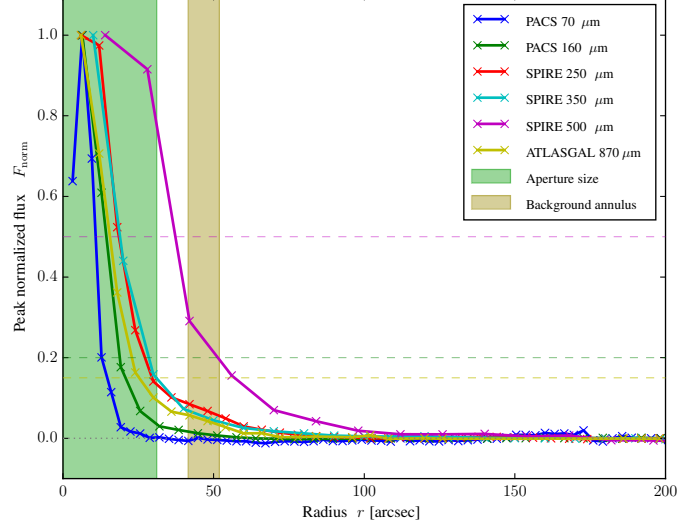


Fig. 6. Emission profiles of a single source (AGAL317.867–00.151) for the different bands, showing the aperture (green shaded area) and background annulus (ochre shaded area). The horizontal dashed lines shown in yellow, magenta and green indicate the flux uncertainties we assume for the ATLASGAL, SPIRE $500\ \mu\text{m}$ and remaining *Herschel* bands, respectively. The $500\ \mu\text{m}$ band traces the more extended emission and we therefore assume a measurement uncertainty of 50% in this band when fitting the SEDs.

measurement uncertainty of 20% and a measurement uncertainty of 15% for the flux estimate of the ATLASGAL band. Finally, the absolute calibration uncertainties are added to the intrinsic measurement error in quadrature to obtain the uncertainties of the (non-saturated) flux densities.

3.3. SED models

The multi-wavelength photometric data obtained were fitted using standard methods to obtain the dust temperature and bolometric luminosity of each source.

For sources for which no mid-infrared emission is detected (or a flux density measurement is available for only one mid-infrared band), we follow the method of Elia et al. (2010) and Motte et al. (2010), fitting a single graybody model to the flux densities measured for the cold dust envelope. When fitting only the cold component, we use the $70\ \mu\text{m}$ flux density as an upper limit for the dust emission. Assuming the measured flux density at $70\ \mu\text{m}$ is always a combination from the cold dust envelope and a young embedded object, taking it as an upper limit for the dust emission avoids overestimating the dust temperature. For the fitting of the graybody we leave the dust spectral index β fixed to a value of 1.75, computed as the mean value from the dust opacities over all dust models of Ossenkopf & Henning (1994) for the submm regime. This also facilitates comparison of the envelope masses calculated here with previous results presented in the literature (e.g., Thompson et al. 2004; Nguyen Luong et al. 2011).

Where at least two flux density measurements are available at the (different) shorter wavelengths, a two-component model consisting of a blackbody and a graybody is fitted to the SED (e.g., Beuther et al. 2010). As the $70\ \mu\text{m}$ flux has a significant influence on the general quality of the fit (Mottram et al. 2011b) and hence on the temperature estimate of the cold dust, the blackbody being added to the model quantitatively constrains the contribution of a deeply embedded, hot component to the $70\ \mu\text{m}$ flux density. For the mid-infrared weak sources a flux density measurement at $21\ \mu\text{m}$ might be available, but as at least two measurements are necessary for the hot component to be fitted, only the graybody is taken into account, emphasizing the importance of the $70\ \mu\text{m}$ flux being taken as an upper limit in such cases (compare Fig. 7, second tile).

We were able to fit the SEDs for all 110 sources in our sample. A single graybody component fit was used to model the emission for 38 of the mid-infrared dark sources while the remaining 73 sources were fitted using the two component fit of a graybody plus the blackbody as described in the previous section. In Fig. 7 we show sample SEDs for all four classes and the model fits to the data. The top panels show a single component graybody fit to a $70\ \mu\text{m}$ weak and to a mid-infrared weak source, whilst the lower panels show the results of a two component fit to sources of the class of mid-infrared weak sources and the H II regions. A comparison of the two-component model with the radiative transfer model used by Robitaille et al. (2007) is presented in Sect. 4.1.

4. Results

We have obtained estimates for the bolometric dust temperatures and fluxes for the whole sample. Combining these parameters with the distances discussed in Sect. 2, we have calculated the source masses, luminosities and column densities for all but one source. In Tables 1 and 2 we give the parameters for each source and a summary of the derived parameters for each class, respectively. Figure 8 presents cumulative distribution functions for the dust temperatures, bolometric luminosities, masses, linear source sizes, and column densities.

We excluded nine sources from the analysis for which the SEDs or classification were unreliable, as the sources are located

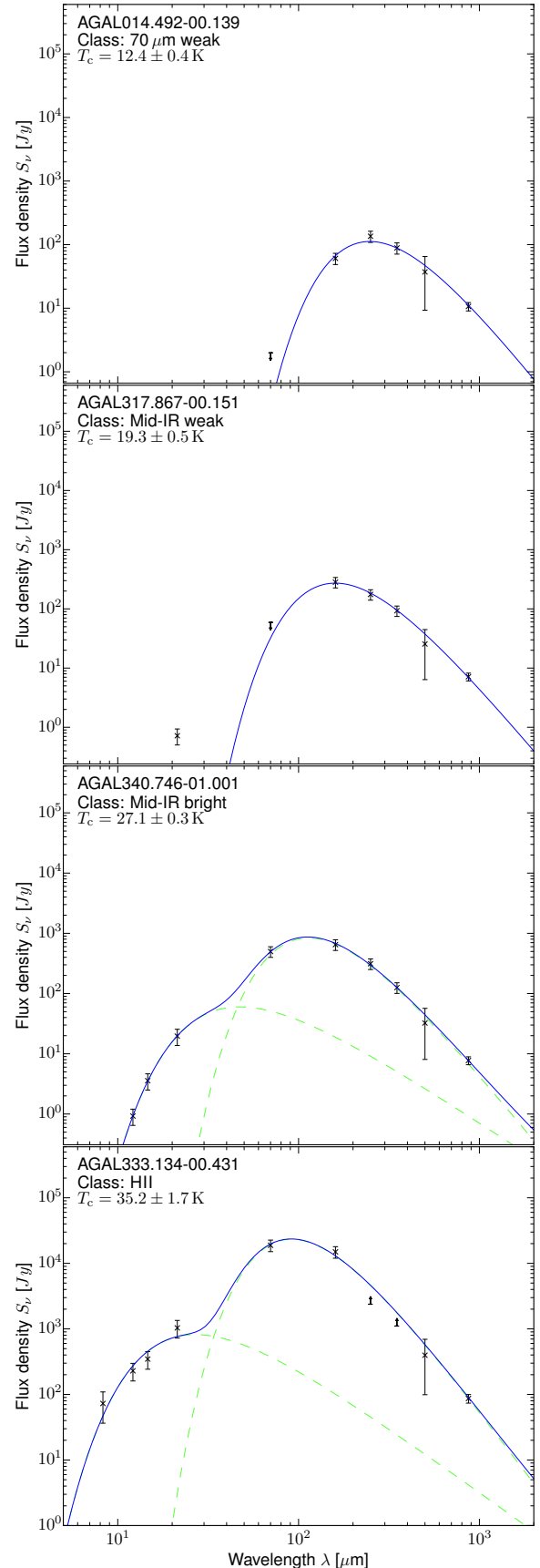


Fig. 7. Sample SEDs for all four evolutionary classes sorted from youngest to most evolved sources *from top to bottom*. A single component graybody is fitted for the upper two, whereas a two-component fit is used for the later two sources. The green dashed lines in the lower panels show the graybody and blackbody components of the fit.

Table 1. Source parameters for the first 15 sources.

Name	d (kpc)	d_{ref}	V_{lsr} (km s $^{-1}$)	l_{app} (deg)	b_{app} (deg)	D_{app} (")	Class	T (K)	ΔT (K)	L_{bol} (L_{\odot})	M_{clump} (M_{\odot})	α_{vir}
AGAL006.216–00.609	2.9	(22)	18.5	6.216	-0.609	71.6	IRw	16.0	0.2	7.3×10^2	4.5×10^2	—
AGAL008.671–00.356	4.8	(19)	35.1	8.668	-0.355	69.1	HII	26.3	1.4	8.6×10^4	3.0×10^3	—
AGAL008.684–00.367	4.8	(19)	38.0	8.682	-0.367	66.1	IRw	24.2	0.2	2.7×10^4	1.4×10^3	0.69
AGAL008.706–00.414	4.8	(19)	39.4	8.704	-0.412	92.1	IRw	11.8	0.3	5.0×10^2	1.6×10^3	0.22
AGAL008.831–00.027	—	—	0.5	8.831	-0.027	70.9	IRw	24.1	1.5	—	—	—
AGAL010.444–00.017	8.6	(1)	75.9	10.442	-0.016	65.5	IRw	20.7	0.3	1.1×10^4	1.6×10^3	0.40
AGAL010.472+00.027	8.6	(1)	67.6	10.472	+0.028	55.1	HII	30.5	2.4	4.6×10^5	1.0×10^4	0.22
AGAL010.624–00.384	5.0	(1)	-2.9	10.623	-0.382	65.0	HII	34.5	3.6	4.2×10^5	3.7×10^3	0.42
AGAL012.804–00.199	2.4	(28)	36.2	12.805	-0.197	84.4	HII	35.1	2.3	2.4×10^5	1.8×10^3	0.78
AGAL013.178+00.059	2.4	(25)	50.4	13.176	+0.062	87.6	70w	24.2	0.8	8.3×10^3	3.6×10^2	0.96
AGAL013.658–00.599	4.5	(22)	48.4	13.656	-0.596	67.0	IRb	27.4	1.3	2.0×10^4	5.6×10^2	0.53
AGAL014.114–00.574	2.6	(3)	20.8	14.112	-0.572	81.0	IRw	22.4	0.8	3.1×10^3	3.5×10^2	0.65
AGAL014.194–00.194	3.9	(3)	39.2	14.194	-0.191	72.0	IRw	18.2	0.6	2.7×10^3	8.2×10^2	0.50
AGAL014.492–00.139	3.9	(3)	39.5	14.491	-0.137	89.3	70w	12.4	0.4	7.5×10^2	1.9×10^3	0.55
AGAL014.632–00.577	1.8	(27)	18.5	14.631	-0.576	83.5	IRw	22.5	0.4	2.7×10^3	2.5×10^2	0.84

Notes. The Columns are as follows: name: the ATLASGAL catalog source name; d : distance; d_{ref} : distance reference (see list of references below table); V_{lsr} : source velocity; l_{app} : Galactic longitude of aperture center; b_{app} : Galactic latitude of aperture center; D_{app} : aperture diameter; Class: class of the source (HII: HII region, IRb: mid-infrared bright, 24d: mid-infrared weak (c: confused within the aperture), 70d: 70 μm weak); T : dust temperature; ΔT : error of the dust temperature; L_{bol} : bolometric luminosity; M_{clump} : clump mass; α_{vir} : virial parameter. All data (including fluxes) will be available in electronic form on the ATLASGAL website (<http://atlasgal.mpifr-bonn.mpg.de/top100>) and the CDS.

References. Distance references: (1): Sanna et al. (2014); (2): Zhang et al. (2014); (3): Giannetti et al. (2014); (4): Zhang et al. (2013); (5): Brunthaler et al. (2009); (6): Giannetti et al. (2015); (7): Giannetti et al. (2014); (8): Sato et al. (2014); (9): Xu et al. (2011); (10): Sato et al. (2010); (11): Urquhart et al. (2012); (13): Moisés et al. (2011); (14): Busfield et al. (2006); (15): Snell et al. (1990); (16): Davies et al. (2012); (17): Tangent Point; (18): Roman-Duval et al. (2009); (19): Green & McClure-Griffiths (2011); (20): Kurayama et al. (2011); (21): Zhang et al. (2009); (22): Wienen et al. (2015); (23): Urquhart et al. (2014b); (24): Xu et al. (2009); (25): Immer et al. (2013); (26): Caswell et al. (1975); (27): Wu et al. (2014); (28): Immer et al. (2012).

in rather complex regions. For four sources (AGAL024.651–00.169, AGAL305.209+00.206, AGAL338.926+00.554, and AGAL354.944–00.537) the aperture is cutting into some nearby source and hence overestimating the background corrected flux. For three sources (AGAL008.706–00.414, AGAL022.376+00.447, and AGAL351.161+00.697) the background aperture is picking up some broad emission, leading the source flux to be underestimated. For AGAL028.564–00.236 the region within the aperture is too complex to be interpreted as a single source and AGAL013.178+00.059 is located on a background with a strong gradient leading to an unreliable flux estimate. This reduces the sample size for the analysis of evolutionary trends to 101 sources.

Comparing the average values of the parameters for the different source classifications and the cumulative distributions presented in Table 2 and Fig. 8 reveals evidence for evolutionary trends with increases in temperatures, bolometric luminosities, and column densities as a function of the different stages. We also find that the mean masses and linear sizes of the subsamples are similar and so we conclude that the initial conditions were also similar, assuming the clumps not to accrete from a much larger mass reservoir.

4.1. Dust temperature and bolometric luminosity

The dust temperature is a fitted parameter of the modified black-body model. Values range from 11 K for the 70 μm weak sources to 41 K for the H II regions' dust envelopes. The lowest temperatures are close to the temperature expected for quiescent clumps, which is determined by cosmic ray heating (~ 10 K; Urban et al. 2009), consistent with the proposed starless nature of the 70 μm

weak sources. It is worth bearing in mind that these sources are likely to have even lower temperatures in the inner part of the clumps as indicated by Bernard et al. (2010). The mean temperature of the dust envelope increases through the different categories from 16.4 K for the 70 μm weak sources up to a mean temperature of 31.7 K for the HII regions, with an average dust temperature of 24.7 K for the whole sample. We point out that the dust temperatures for the HII regions should be taken with care (and possibly as lower limits) as the emission might be optically thick for a portion of the SED (see, e.g., Elia & Pezzuto 2016).

As can be seen from the cumulative histogram in Fig. 8 (upper left panel), the dust temperature increases with the evolutionary stage and the different classes (and hence evolutionary stages) are well separated with regard to the dust temperature. This is confirmed by Anderson-Darling tests yielding p -values lower than 2.7×10^{-3} for all classes, rejecting the null hypothesis that these are drawn from the same distribution at the 3σ significance level.

To estimate the bolometric luminosities L_{bol} for each source, we combine the distance and integrated flux determined from the fitted SED model using the equation

$$L_{\text{bol}} = 4\pi d^2 \int S_{\lambda} d\lambda, \quad (1)$$

where d is the distance to the source (Sect. 2.2) and $\int S_{\lambda} d\lambda$ is the integrated flux. The bolometric luminosities for the whole sample range from $57 L_{\odot}$ for the least luminous source to $3.8 \times 10^6 L_{\odot}$ for the most luminous H II region, with a mean value of $1.3 \times 10^5 L_{\odot}$ and a median value of $1.5 \times 10^4 L_{\odot}$. The cumulative distribution function of the luminosities shows

Table 2. Overview of the different classes and their parameters.

Class/Parameter	Mean	Median	Min	Max	Standard deviation	Standard error
70 μm weak						
T_{dust}/K	16.4	16.9	10.7	24.24	3.35	0.8
L_{bol}/L_{\odot}	3.2×10^3	2.2×10^3	4.3×10^2	9.1×10^3	2.9×10^3	7.3×10^2
M_{env}/M_{\odot}	2.1×10^3	1.3×10^3	1.2×10^2	1.0×10^4	2.6×10^3	6.4×10^2
$L_{\text{bol}}/M_{\text{env}} \cdot L_{\odot}/M_{\odot}$	3.4	2.6	0.2	22.6	5.1	1.3
r/pc	1.1	1.0	0.4	2.74	0.63	0.2
$N_{\text{H}_2}/\text{cm}^{-2}$	5.6×10^{22}	4.8×10^{22}	2.4×10^{22}	1.3×10^{23}	2.7×10^{22}	6.8×10^{21}
Mid-IR weak						
T_{dust}/K	19.9	21.4	11.7	26.18	4.26	0.7
L_{bol}/L_{\odot}	2.2×10^4	5.7×10^3	5.7×10^1	2.2×10^5	4.1×10^4	7.1×10^3
M_{env}/M_{\odot}	2.2×10^3	1.3×10^3	1.8×10^1	1.1×10^4	2.5×10^3	4.4×10^2
$L_{\text{bol}}/M_{\text{env}} \cdot L_{\odot}/M_{\odot}$	8.3	7.2	0.3	25.7	7.3	1.3
r/pc	1.0	0.7	0.2	2.49	0.64	0.1
$N_{\text{H}_2}/\text{cm}^{-2}$	1.1×10^{23}	7.6×10^{22}	3.7×10^{22}	7.6×10^{23}	1.3×10^{23}	2.3×10^{22}
Mid-IR bright						
T_{dust}/K	28.1	28.2	21.9	34.53	3.65	0.6
L_{bol}/L_{\odot}	5.0×10^4	2.2×10^4	9.9×10^2	2.5×10^5	5.4×10^4	9.1×10^3
M_{env}/M_{\odot}	1.5×10^3	6.0×10^2	1.8×10^1	9.1×10^3	2.3×10^3	3.8×10^2
$L_{\text{bol}}/M_{\text{env}} \cdot L_{\odot}/M_{\odot}$	51.2	37.6	7.5	150.0	38.1	6.4
r/pc	0.6	0.6	0.2	2.45	0.41	0.1
$N_{\text{H}_2}/\text{cm}^{-2}$	1.7×10^{23}	7.4×10^{22}	3.2×10^{22}	7.8×10^{23}	1.8×10^{23}	3.0×10^{22}
HII regions						
T_{dust}/K	31.7	31.8	22.8	41.12	3.97	0.8
L_{bol}/L_{\odot}	4.6×10^5	2.0×10^5	3.0×10^3	3.8×10^6	7.7×10^5	1.5×10^5
M_{env}/M_{\odot}	6.0×10^3	2.1×10^3	2.8×10^2	4.3×10^4	9.0×10^3	1.8×10^3
$L_{\text{bol}}/M_{\text{env}} \cdot L_{\odot}/M_{\odot}$	86.7	75.5	10.8	358.8	67.4	13.5
r/pc	0.8	0.7	0.2	1.89	0.47	0.1
$N_{\text{H}_2}/\text{cm}^{-2}$	3.6×10^{23}	2.6×10^{23}	1.3×10^{23}	1.1×10^{24}	2.1×10^{23}	4.2×10^{22}
All						
T_{dust}/K	24.7	24.7	10.7	41.12	6.85	0.7
L_{bol}/L_{\odot}	1.3×10^5	1.6×10^4	5.7×10^1	3.8×10^6	4.1×10^5	3.9×10^4
M_{env}/M_{\odot}	2.8×10^3	1.2×10^3	1.8×10^1	4.3×10^4	5.1×10^3	4.9×10^2
$L_{\text{bol}}/M_{\text{env}} \cdot L_{\odot}/M_{\odot}$	39.7	22.5	0.2	358.8	50.7	4.8
r/pc	0.9	0.7	0.2	2.74	0.56	0.1
$N_{\text{H}_2}/\text{cm}^{-2}$	1.8×10^{23}	8.6×10^{22}	2.4×10^{22}	1.1×10^{24}	1.9×10^{23}	1.8×10^{22}

Notes. Given are the mean, median, minimum, maximum, standard deviation, and standard error for each parameter.

that they increase with the evolutionary stage yielding p -values $< 2.4 \times 10^{-5}$ for the Anderson-Darling test. However, these tests reveal no significant difference between the mid-infrared weak and mid-infrared bright samples (p -value = 1.2×10^{-2}) as well as between the mid-infrared weak and the 70 μm weak sources (p -value = 5.6×10^{-3}).

To verify that the extraction of the photometry and the use of a relatively simple two-component model to fit the SED produces reliable results, we compare our derived luminosities with those reported for a subsample of the same sources reported by the RMS team (Urquhart et al. 2014b). This other research has used fluxes drawn from the Hi-GAL point source catalog (Molinari et al. 2016), and the more complex radiative transfer models determined by Whitney et al. (2005) and the fitting tool developed by Robitaille et al. (2007). In Fig. 9 we show this comparison of the bolometric luminosities for 41 matching sources of the RMS sample. It is clear from this plot that there is good agreement between these two very different methods.

4.2. Clump mass, size, and column density

To estimate the masses of the sources we followed the procedure of Hildebrand (1983) for an optically thin emission and a single temperature, as the derived optical depth at 870 μm is $\tau_{870} \ll 1$ for all sources:

$$M_{\text{clump}} = \frac{d^2 S_{870} R}{B_{870}(T_d) \kappa_{870}}, \quad (2)$$

where d is the distance to the cloud, S_{870} is the integrated 870 μm flux density obtained from the aperture photometry, R is the gas-to-dust ratio assumed to be 100, $B_{870}(T_d)$ is the intensity of the blackbody at 870 μm at the dust envelope temperature T_d , and $\kappa_{870} = 1.85 \text{ cm}^2 \text{ g}^{-1}$ is the dust opacity at 870 μm calculated as the average of all dust models from Ossenkopf & Henning (1994) for the dust emissivity index of 1.75 that we use for the fitting of the SEDs.

The derived clump masses range from $18 M_{\odot}$ up to $4.3 \times 10^4 M_{\odot}$, with a mean value of $2.8 \times 10^3 M_{\odot}$ and a median value

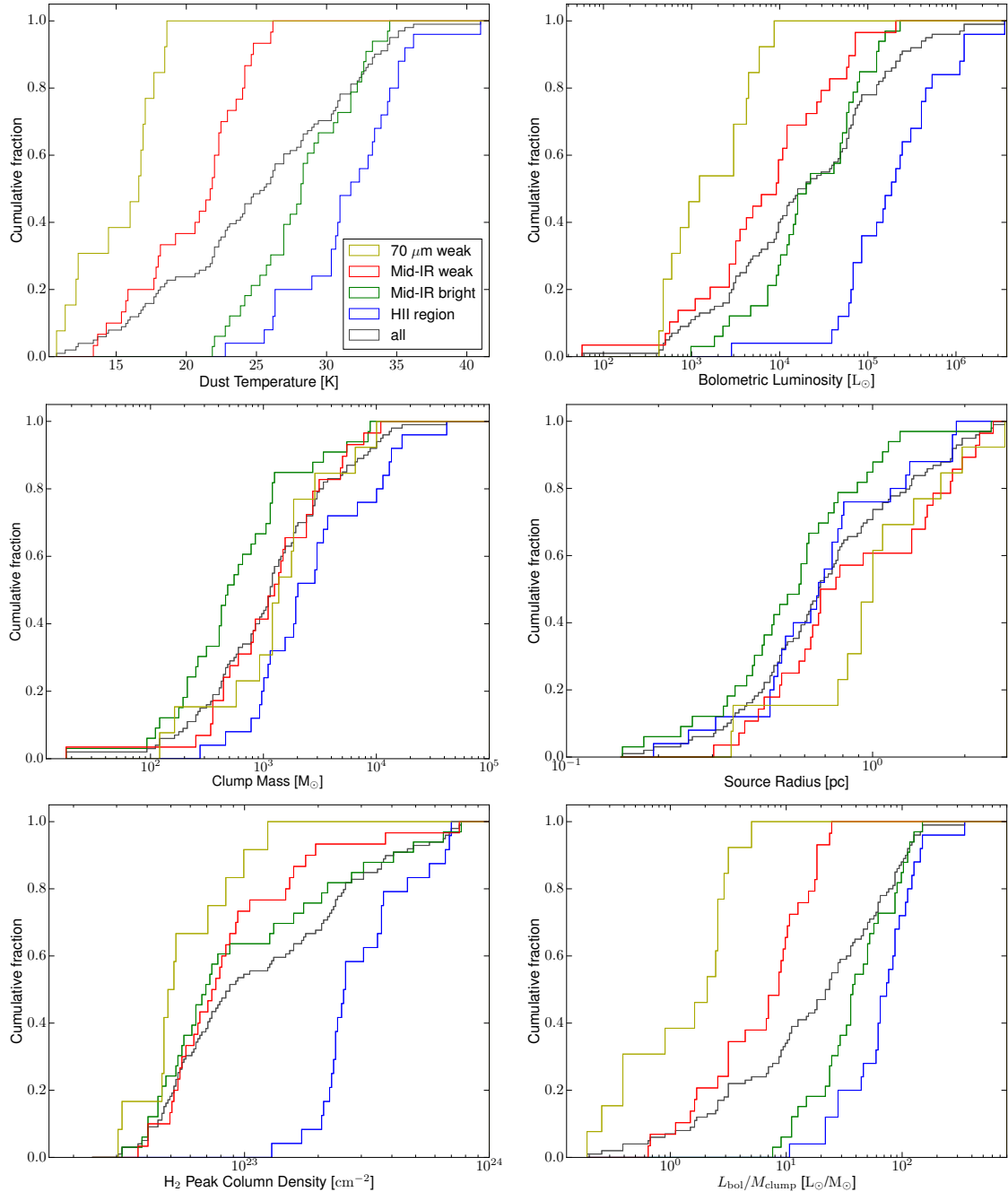


Fig. 8. Cumulative distribution plots showing the range of values for the derived parameters for the whole sample (grey curve) and the four evolutionary sub-samples (see legend for colours).

of $1.2 \times 10^3 M_\odot$ for the whole sample. Two sources are found to have comparatively low masses (AGAL316.641–00.087 and AGAL353.066+00.452), making them unlikely to form any massive stars. The mass cumulative distribution plot shown in Fig. 8 (mid-left panel) reveals little variation between the different classes and is therefore relatively independent of the evolutionary phase. This is confirmed by Anderson-Darling tests with only the mid-infrared bright and HII regions yielding a p -value of 1.0×10^{-4} making them unlikely to be drawn from the same distribution. We note that this difference is likely to be an effect of the dust temperatures being lower limits for the compact HII regions (see Sect. 4.1) and hence the envelope masses being upper limits.

The linear size of a source (i.e., its radius r) in pc can be calculated from the distance D in pc and the deconvolved source size θ_{deconv} as

$$r = d \cdot \tan(\theta_{\text{deconv}}/2), \quad (3)$$

with the deconvolved size of the source being calculated as

$$\theta_{\text{deconv}} = \sqrt{D_{\text{ap}}^2 - \theta_{\text{beam}}^2}, \quad (4)$$

where D_{ap} is the source size as used for the aperture and θ_{beam} is the FWHM size of the beam (i.e., $19.2''$). The cumulative distribution of the linear source size is presented in the middle

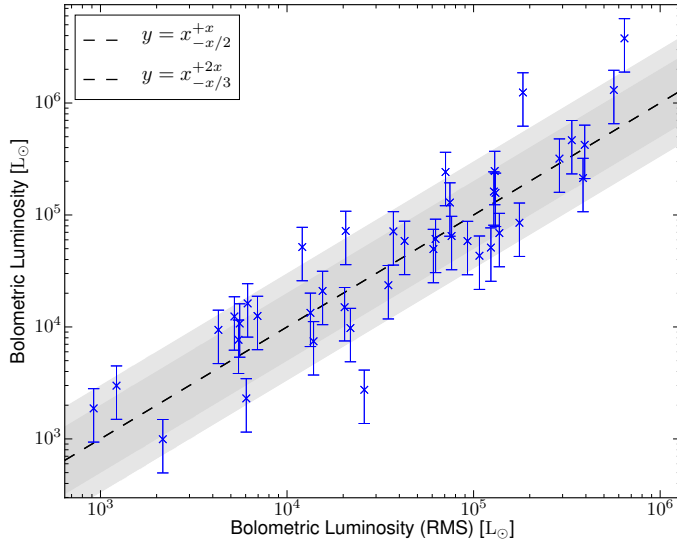


Fig. 9. Comparison of our luminosities to those of Urquhart et al. (2014b) for sources common in both studies. The gray shaded areas indicate the area of an agreement within a factor of two (dark) and three (light). Most of the luminosities agree within a factor of three, showing that our simplified two-component model is sufficient to get an estimate for the luminosity.

right panel of Fig. 8, with a mean value of 0.9 pc and a median value of 0.7 pc over all classes. We find mostly no significant differences between the different evolutionary classes, with Anderson-Darling tests all yielding p -values > 0.003 , except between the mid-infrared bright and the 70 μm weak sources (p -value = 2.6×10^{-3}).

We also calculate the beam averaged column density according to Schuller et al. (2009), assuming the dust emission at 870 μm is optically thin:

$$N_{\text{H}_2} = \frac{F_{870} R}{B_{870}(T_{\text{d}}) \Omega_{\text{app}} \kappa_{870} \mu_{\text{H}_2} m_{\text{H}}}, \quad (5)$$

where F_{870} being the peak flux density, the beam solid angle Ω_{app} , and $\mu_{\text{H}_2} = 2.8$ as the mean molecular weight of the interstellar medium with respect to a hydrogen molecule according to Kauffmann et al. (2008), and m_{H} the mass of a hydrogen atom. The other parameters are as previously defined.

In Fig. 8 (lower left panel) we show the histogram of the beam averaged peak column densities. The mean column density increases from $2.4 \times 10^{22} \text{ cm}^{-2}$ for the 70 μm weak sources to column densities in excess of 10^{24} cm^{-2} for the HII regions. This is to be expected, as the clumps increase their density in the process of collapse. We note that the class of compact HII regions is well distinguished from the other classes, being confirmed by Anderson-Darling tests (p -values $< 2.4 \times 10^{-5}$). We point out that the column densities are effected by the dust temperatures being lower limits for the compact HII regions as discussed in Sect. 4.1, hence rendering the column densities upper limits. Furthermore, this nicely shows that the young HII regions have not dispersed the envelope significantly yet, as we would expect for the sources being selected to be the brightest in ATLASGAL, hence making them the densest phase before dispersing the dust envelopes. For the other classes the null-hypothesis of the samples being drawn from the same distribution cannot be rejected with p -values $> 1.1 \times 10^{-2}$. However, taking a closer look at the cumulative distribution of the column density in Fig. 8 (lower left plot) and taking into account the small number of

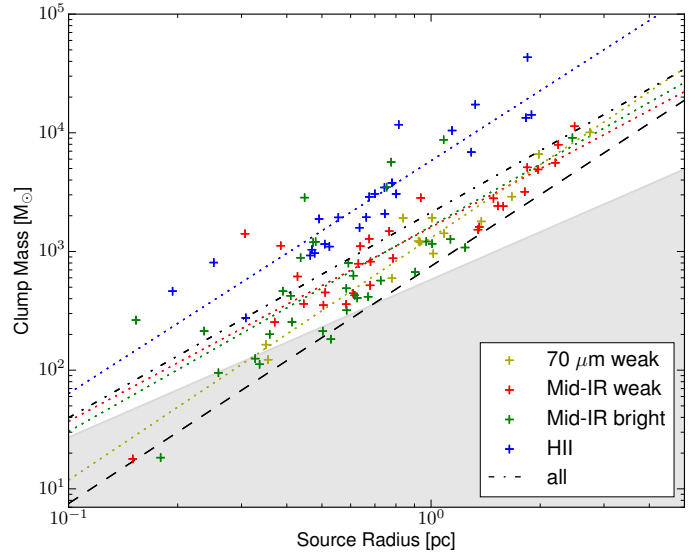


Fig. 10. Mass-size relationship of the ATLASGAL Top100. The lower right gray shaded area highlights the region where it is unlikely that high-mass stars are formed according to Kauffmann et al. (2010) and the black dashed line indicates a surface density of 0.05 g cm^{-2} determined as the lower limit for efficient massive-star formation by Urquhart et al. (2014c). The slopes of the linear log-log fits of all classes agree with each other within the margin of error of the fitted power laws.

only 16 source of the 70 μm weak sample, we speculate that this subclass might be well distinguishable for a larger sample.

5. Discussion

5.1. Comparison with massive-star formation relations

In Fig. 10 we present the mass-size relation for the sample. According to Kauffmann et al. (2010), a lower limit for high-mass star formation is given by $M(r) \geq 580 M_{\odot} \cdot (r/\text{pc})^{1.33}$ when reducing the mass coefficient by a factor of 1.5 from 870 to 580 to match with the dust absorption coefficient used in the present paper. Taking this threshold as the lower limit for massive-star formation, we find that 93 (i.e., 85%) of our sources have the potential to form at least one massive star. Similarly assuming the threshold found by Urquhart et al. (2014c), indicating that sources with surface densities above 0.05 g cm^{-2} can efficiently form high-mass stars, up to 99 sources (i.e., 98% of the sources with good SEDs and classification) have already formed at least one high-mass star or are likely to do so in the future.

To estimate the stability of the clumps, we calculate the virial parameter for the 102 sources of Giannetti et al. (2014), but correct for the revised distances d . Revising the distances affects the linear source sizes r_{FWHM} for the regions for which the velocity dispersion was measured (i.e., approximately the FWHM of the source). We calculate the virial parameter according to Bertoldi & McKee (1992):

$$\alpha_{\text{vir}} = \frac{5}{G} \cdot \left(\frac{\Delta V}{2 \sqrt{2 \ln 2}} \right)^2 \cdot r_{\text{FWHM}} \cdot M_{\text{clump}}^{-1}, \quad (6)$$

where we adopted the C¹⁷O (3–2) linewidth ΔV in km s^{-1} from Giannetti et al. (2014), G the gravitational constant and M_{clump} the clump mass estimated from the flux given by Csengeri et al. (2014) using Eq. (2). Here the linewidth and the envelope mass are estimated using the FWHM source sizes. The result is shown in Fig. 11.

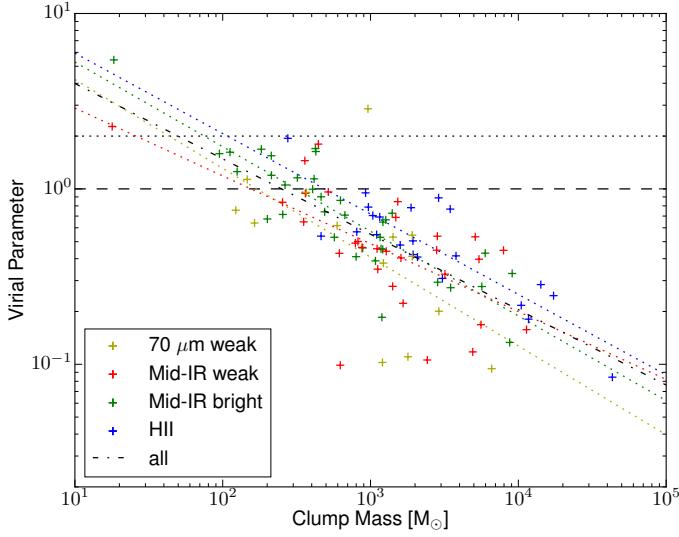


Fig. 11. Clump mass versus virial parameter α_{vir} . The dashed and dotted lines represent $M_{\text{vir}} = M_{\odot}$ and $M_{\text{vir}} = 2 M_{\odot}$, respectively. Sources below these lines are likely to be unstable and hence collapsing with and without a magnetic field being present (represented by the dashed and dotted lines, respectively).

In general, we see a similar anti-correlation of the clump mass with the virial parameter as reported in other works (e.g., Kauffmann et al. 2013; Urquhart et al. 2014c; Giannetti et al. 2014), indicating that stability of clumps decreases as their mass increases. Fitting a power law to the data for all classes, we find the trend of all classes to be very similar to each other, with a general slope of $s = -0.43 \pm 0.04$ for the whole sample (compare Fig. 11).

Kauffmann et al. (2013) adopted a critical value of $\alpha_{\text{crit}} = 2$ for a Bonnor-Ebert sphere (Bonnor 1955) not being supported by a magnetic field. Under this assumption a clump is likely to be unstable if $\alpha_{\text{vir}} < 2$. From this we conclude that at least 99 sources (i.e., 97%) are likely to be unstable.

For the whole sample only three sources show a virial parameter of $\alpha_{\text{vir}} > 2$ (AGAL316.641–00.087, AGAL338.066+00.044, and AGAL353.066+00.452) and are therefore unlikely to be collapsing, if external pressure does not confine them. Two of these sources (AGAL316.641–00.087 and AGAL353.066+00.452) with a virial parameter of $\alpha_{\text{vir}} \approx 5.4$ and 2.3, respectively, were found to have masses lower than $19 M_{\odot}$ making them unlikely to form a massive star.

In case of a magnetic field being present, Bertoldi & McKee (1992) showed that with the magnetic field and kinetic support being equal, the critical value of the virial parameter is lower ($\alpha_{\text{crit}} = 1$). Taking this lower critical parameter as the threshold for collapse, we find that 84 of the sources (i.e., 82%) are gravitationally unstable and in the absence of strong magnetic fields are likely to be collapsing.

To further investigate the minimum magnetic field strength needed to support the clumps against gravitational collapse, we follow the procedure of Kauffmann et al. (2013), calculating the critical field strength as

$$B_{\text{crit}} = 81 \mu\text{G} \cdot \frac{M_{\Phi}}{M_{\text{BE}}} \left(\frac{\Delta V}{2 \sqrt{2 \ln 2}} \right)^2 \frac{1}{r_{\text{FWHM}}}, \quad (7)$$

where we substitute

$$\frac{M_{\Phi}}{M_{\text{BE}}} = \frac{2}{\alpha_{\text{vir}}} - 1 \quad (8)$$

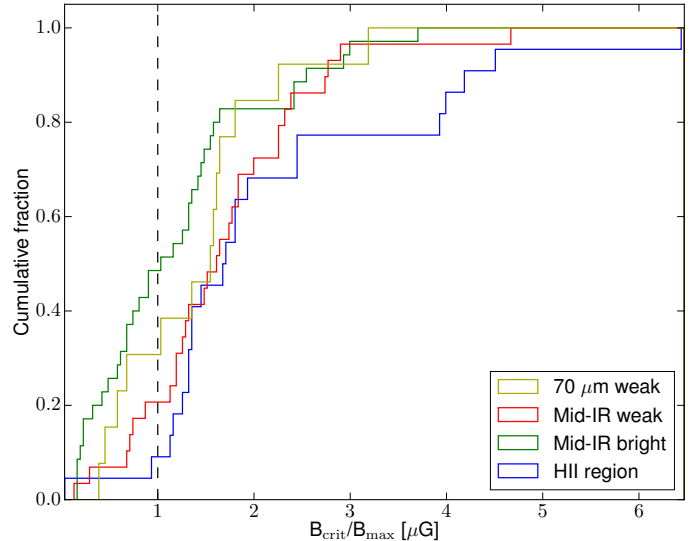


Fig. 12. Ratio of the minimum critical magnetic field strength needed to stabilize our sources B_{crit} to the upper limit magnetic field strength B_{max} for a cloud as suggested by Crutcher (2012). Sources right of the dashed line ($B_{\text{crit}} = B_{\text{max}}$) cannot build a magnetic field strong enough to prevent the clumps from collapsing.

as calculated from the virial parameter α_{vir} . We find the median critical field strength to range from 0.8 mG for the 70 μm weak class up to 6.2 mG for the compact HII regions. Crutcher (2012) proposes a density-dependant upper limit for the magnetic field strength in a molecular cloud of

$$B_{\text{max}} = 10 \mu\text{G} \left(\frac{n_{\text{H}_2}}{150 \text{ cm}^{-3}} \right)^{0.65}, \quad (9)$$

implying that if $B_{\text{crit}} > B_{\text{max}}$ no existing magnetic field can stabilize the cloud. To apply our data, we further transform Eq. (9) as shown by Kauffmann et al. (2013, C.4) into

$$B_{\text{max}} = 336 \mu\text{G} \left(\frac{M_{\text{clump}}}{10 M_{\odot}} \right)^{0.65} \left(\frac{r_{\text{FWHM}}}{0.1 \text{ pc}} \right)^{-1.95}. \quad (10)$$

Comparing B_{crit} to B_{max} (see Fig. 12) we find the minimum magnetic field strength needed to stabilize our sources to be higher than the upper limit suggested by Crutcher (2012) for 69% of our sample. From this we conclude that the majority of our sources can either not be stabilized or would need extreme magnetic fields to support them against gravitational collapse.

Our analysis has revealed that there is no significant difference in the global properties of the sample, with similar mass and size distributions found for all of the sub-samples. It is likely therefore, that they had similar initial physical conditions. We have also found that the majority of the sample satisfies the mass-size threshold criterion required for massive-star formation and that they are unstable to gravity and likely to collapse in the absence of a strong magnetic field, clearly confirming that the sources of the ATLASGAL Top100 are a sample of massive-star forming regions.

5.2. Evolutionary sequence of the sample

The analysis presented in the previous subsection found little difference in the masses and stability of the various subsamples and revealed them all to be good candidates for massive-star formation. The results obtained from the SED fitting show trends

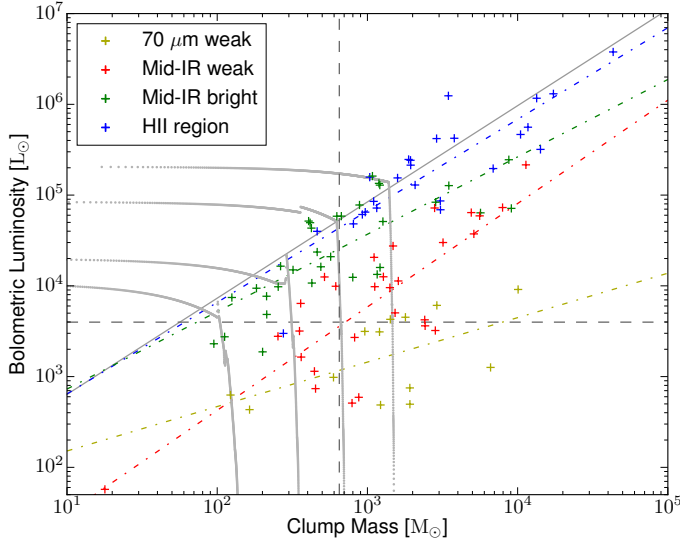


Fig. 13. Mass-luminosity distribution of the whole sample. The gray tracks are evolutionary models used by Molinari et al. (2008). The dash-dotted colored lines show a linear fit to the corresponding class of sources. The horizontal dashed line shows the luminosity of a B1.5 star as calculated by Mottram et al. (2011a, Table 1), whereas the vertical dashed line shows the threshold of $650 M_{\odot}$ beyond which clumps are likely to host massive dense clumps or high-mass protostars (Csengeri et al. 2014).

for increasing temperatures and bolometric luminosity that are consistent with the proposed evolutionary sequence. In this subsection we will extend this analysis in order to robustly test the evolutionary scheme of the ATLASGAL Top100.

Following the procedure of Molinari et al. (2008), we compare here the clump mass versus the bolometric luminosity (Fig. 13). In such a plot it is expected that clumps first gain luminosity, moving upward in the plot until the embedded stars reach the zero age main sequence (ZAMS, solid diagonal line) and then lose mass, as the dust envelope gets dispersed, moving leftward in the plot (compare with Molinari et al. 2008). It can be seen that the earlier evolutionary stages (i.e., the $70 \mu\text{m}$ and mid-infrared weak sources) follow this trend clearly toward the zero age main sequence. The later stages (i.e., the mid-infrared bright and HII regions) are not as well separated, making it difficult to distinguish their evolutionary stage from dust emission alone, consistent with the findings of Urquhart et al. (2014c).

Fitting a power law to the data for all four classes, we find that for the HII regions, mid-infrared bright and weak sources the trend is very similar, yielding slopes of $s = 1.01 \pm 0.13$, $s = 0.85 \pm 0.13$ and $s = 1.14 \pm 0.16$, respectively. These values are lower than those reported by Molinari et al. (2008) and Urquhart et al. (2014c), but still in agreement within 3σ . Only the sample of $70 \mu\text{m}$ weak sources yields a slightly lower slope of $s = 0.49 \pm 0.24$, which, however, is still in agreement with the slopes of the other samples. The low number of sources in this subsample could result in the fit being significantly affected by incomplete sampling and/or outliers. Nevertheless, the positions of the subsamples seen in the mass-luminosity plot are consistent with the expected evolutionary tracks and nicely illustrate that our sample covers a wide range of evolutionary stages.

Given that early B-type stars have a minimum luminosity of $\sim 10^{3.6} L_{\odot}$ (Mottram et al. 2011a, Table 1), we can see from the mass-luminosity distribution (Fig. 13) that a large proportion (80 sources, i.e. 73%) of our sample already has luminosities in

excess of this threshold. As the luminosity of a cluster is dominated by the most massive star, it is likely that these clumps have already formed at least one high-mass star. Csengeri et al. (2014) take a mass limit of $650 M_{\odot}$ for clumps likely to form high-mass protostars, and 73 sources (i.e., 66%) are found above this limit. Taking into account both aforementioned thresholds ($L_{\text{bol}} > 10^{3.6} L_{\odot}$ and $M_{\text{clump}} > 650 M_{\odot}$), it is therefore likely that at least 93 sources (i.e., 85% of our sample) have either already formed or will likely go on to form a cluster consisting of at least one massive star in the future.

To further investigate the evolutionary stage of the sources, we present the cumulative histogram of the bolometric luminosity to clump mass ratio in Fig. 8 (lower right panel). This ratio is a crude proxy for the evolutionary stage and we would therefore expect this to increase as the embedded objects evolve and become more luminous. This plot clearly shows a trend for increasing $L_{\text{bol}}/M_{\text{clump}}$ ratio with evolution, increasing continuously from a minimum ratio of 0.2 for the $70 \mu\text{m}$ weak sources up to a ratio of 358.8 for the HII regions. Performing Anderson-Darling tests, we find that almost all evolutionary stages are clearly distinct from each other, yielding p -values $< 3.6 \times 10^{-4}$, rejecting the null-hypothesis of the samples being drawn from the same distribution at the 3σ significance level. We only find the mid-infrared bright and HII region phases to be similar enough, as to be drawn from the same distribution with a p -value of 2.6×10^{-2} .

5.3. Dust continuum emission as evolutionary stage indicator

As we have seen in the previous sections, the physical parameters and derived quantities obtained from dust continuum emission (namely temperature, bolometric luminosity, clump mass, $L_{\text{bol}}/M_{\text{env}}$, linear source size, or column density) are differently well suited to distinguish between the evolutionary phases of massive-star formation.

In Table 3 we give an overview of whether or not the Anderson-Darling tests are able to distinguish two evolutionary stages of our sample using the given parameter. We note that except for the temperature no single parameter is suited to discriminate between all evolutionary stages alone. However, all classes can be well distinguished by a combination of at least two different parameters and the evolutionary sequence is well reflected in the physical parameters obtained from the dust emission. But although there are clear trends seen in the distributions of some of the derived parameters, there is also significant overlap between them (compare Table 2). In turn this makes it impossible to assign a given source to a single evolutionary stage just from the dust parameters and further criteria are required.

The optical depth might limit the usability of the dust emission in extreme cases, where the emission being optically thick at far-infrared wavelengths would underestimate the fluxes of the SED. Similarly the estimated dust temperature might be underestimated for sources for which the emission longward of $\lambda > 21 \mu\text{m}$ becomes optically thick (Elia & Pezzuto 2016). Both effects likely play an important role for the more evolved sources, making the derived physical parameters less reliable for the densest and most evolved sources.

Comparison of extinction properties of low-mass and high-mass clouds and cores have shown that only modest extinctions are required for a core to manifest as infrared dark (Pillai 2016). In a forthcoming work, we show that at the distance of a few kpc, dust emission alone cannot reveal populations of low-mass protostars (Class 0 and higher) embedded within clouds and line observations are crucial in distinguishing such cores from those that are genuinely quiescent (Pillai et al., in prep.). This is further

Table 3. Overview of different physical parameters and whether or not the Anderson-Darling test is able to distinguish the different classes of sources.

Parameter	HII	HII	HII	Mid-IR bright	Mid-IR bright	Mid-IR quiet
	Mid-IR bright	Mid-IR quiet	70 μm weak	Mid-IR quiet	70 μm weak	70 μm weak
T	+	+	+	+	+	+
L_{bol}	+	+	+	-	+	-
M_{env}	+	-	-	-	-	-
$L_{\text{bol}}/M_{\text{env}}$	-	+	+	+	+	+
r	-	-	-	-	+	-
N_{H_2}	+	+	+	-	-	-

supported by recent analysis by [Feng et al. \(2016\)](#) and [Tan et al. \(2016\)](#), who have reported a bipolar outflow of a high-mass protostellar associated with a 70 μm dark source. As outflows are associated with ongoing star formation, this source as well as the analysis presented by [Pillai \(2016\)](#) are good examples of the possible limitations of the dust classification when no source is detected at 70 μm .

Accordingly, the ATLASGAL team is investigating a wide range of molecular line tracers as well as different masers for their suitability as evolutionary stage indicators to supplement the rather rough discrimination obtained from the dust continuum parameters. An overview of these projects will be given in the next section.

5.4. Complementary molecular observations

Molecular lines can be used to independently derive and investigate the physical and chemical properties of the gas in star-forming regions. In the radio (centimeter to millimeter wavelengths) regime, extinction is in general negligible and it is therefore easier to see directly the effect of protostellar activity (e.g., outflows, gas warm-up and hot cores) in molecular lines. Here we discuss the effects of mechanical and thermal feedback as probed by different tracers available for the Top100 sample, synthesizing the results of various studies of methanol and water masers as well as thermal emission from high density molecular tracers in terms of temperature evolution and probes of star formation activity.

Thermal feedback: CO depletion as a function of evolution was investigated by [Giannetti et al. \(2014\)](#). The abundance of CO is correlated with the evolutionary stages in the low-mass regime ([Caselli et al. 1998](#); [Bacmann et al. 2002](#)). In the Top100 we find the same trend: CO depletion decreases in more evolved clumps as a function of L/M , indirectly showing that the sources become warmer with time. The revised classification proposed here does not affect these earlier results. We also find that the C¹⁷O(3–2) linewidth used in Sect. 5.1 increases with evolutionary stage from a median value of 2.2 km s⁻¹ for the 70 μm weak class to 5.3 km s⁻¹ for the compact HII regions under the new classification, confirming the earlier results and further bolstering the evolutionary sequence presented here.

Acetonitrile (CH₃CN) and methyl acetylene (CH₃CCH) are reliable thermometers of the gas. Acetonitrile and methyl acetylene, as well as methanol, will be discussed in detail by Giannetti et al. (in prep.), where preliminary results give further support for our revised classification scheme.

Furthermore, we searched for Class II methanol maser associations in the MMB survey ([Urquhart et al. 2013a](#)). Class II

Table 4. Association with Class II methanol and H₂O masers.

Class	Number ^a of sources	MMB assoc.	MMB ratio	HOPS assoc.	HOPS ratio
70 μm weak	16/10	1	0.06	1	0.10
Mid-IR weak	34/27	17	0.50	15	0.56
Mid-IR bright	36/17	28	0.78	14	0.82
H II region	25/17	20	0.80	11	0.65

Notes. ^(a) The first number gives the number of sources within the region covered by the MMB while the second number gives the number of sources covered by HOPS.

methanol masers are radiatively pumped and therefore trace the radiation field from the central object. We found associations for 66 clumps, with seven clumps being associated with two or more methanol masers. A detailed study of the properties of methanol-maser-associated clumps for the whole ATLASGAL survey is presented in [Urquhart et al. \(2013a\)](#), which includes 55 of the Top100 clumps. The remaining 12 clumps matched with MMB sources are new and have resulted from comparison with the final part of the MMB catalog recently published in [Breen et al. \(2015\)](#). The overall association rate between the Top100 and the MMB catalog is $\sim 63\%$, however, the association rate is significantly higher for the more evolved clump classifications as can be seen in Table 4. The association ratio is similar for the mid-infrared bright and compact HII region classes but drops to $\sim 50\%$ for the mid-infrared weak sources and to close to zero for the 70 μm weak sources. We find $\sim 72\%$ (i.e., 48/66) of all sources associated with a methanol maser to be either mid-infrared bright clumps or compact HII regions. The only 70 μm weak source with maser activity is AGAL013.178+00.059 (Fig. 14). This source is removed from the SED analysis as discussed in Sect. 4. AGAL013.178+00.059 is located near the edge of an evolved HII region and is likely being externally heated and undergoing compression on one side. The external heating has resulted in some extended 70 μm emission that has made a definitive classification more difficult. Although care needs to be taken in the interpretation of the association between this clump and the masers, it does suggest that star formation may already be underway in some of these 70 μm weak clumps. This is further supported by the fact that a water maser is detected in the source (see discussion below).

[Gallaway et al. \(2013\)](#) examined the mid-infrared emission towards a larger sample of 776 methanol masers and found a similar fraction associated with mid-infrared emission. This suggests that methanol masers are associated with more evolved stages where the embedded objects are already producing significant luminosity and have started to warm their local environments. This also ties in nicely with a recent study of

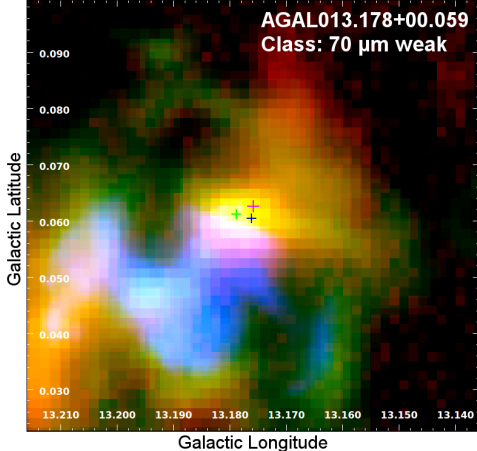


Fig. 14. Three-color image of the $70\text{ }\mu\text{m}$ weak source AGAL013.178+00.059. We note the strong heating from the south east. The magenta, green, and blue crosses mark the positions of the source peak, the associated methanol and water maser, respectively. Size: $\sim 3' \times 3'$; red: ATLASGAL $870\text{ }\mu\text{m}$; green: PACS $160\text{ }\mu\text{m}$; blue: PACS $70\text{ }\mu\text{m}$.

outflows towards methanol masers (de Villiers et al. 2014, 2015) which found that the dynamical age of outflows associated with methanol masers are older than for the general population of molecular outflows reported in the literature.

Mechanical feedback: Standard tracers of outflow activity are, for example, high-velocity line-wings in CO and SiO lines, as well as water masers.

From the ATLASGAL Top100 sample, 36 sources lie in the 1st Galactic quadrant, and are part of the sources investigated by Csengeri et al. (2016). All of them are detected in the SiO(2–1) and (5–4) transitions except for two mid-infrared weak sources. Line-wings are detected altogether towards 21 sources, including three clumps which are dark at $70\text{ }\mu\text{m}$, demonstrating that molecular lines can be a more sensitive probe of star formation activity than dust alone. In a forthcoming paper Navarete et al. will extend the analysis on the content of molecular outflows in the Top100 sample, using observations in the Mid- J CO lines to further test the classification scheme.

We have also searched for position coincidences with water masers identified by the H₂O Southern Galactic Plane Survey (HOPS; Walsh et al. 2011, 2014). This survey covers Galactic longitudes $300^\circ < \ell < 30^\circ$ and Galactic latitudes $|b| < 0.5^\circ$ and so only includes 71 of the Top100 sources. In Table 4 we give the number of sources, the number of these associated with water masers, and the fractional association rates for each evolutionary type. There is a clear trend for increasing frequency of association with water masers with the first three evolutionary stages. This is in agreement with the evolutionary scheme based on the dust analysis. Comparing the water maser association rates with the methanol maser association rates for the different stages, we find them to be similar for the earliest three stages, but the water maser association rate is noticeably lower for the more evolved H II region stage. As water masers can be collisionally excited and hence are an indicator for shocks and outflows, the H₂O maser found for AGAL013.178+00.059 (Fig. 14) can either be associated with material ejection or with compression from the south east, making this an interesting source to investigate possibly in more detail.

To summarize, the results of the molecular line observations as well as the associations between Class II methanol and

H₂O masers support the evolutionary classification scheme outlined in Sect. 2. In particular, the lack of Class II masers towards the $70\text{ }\mu\text{m}$ -dark sources points to the star formation associated with these clumps being in a very early evolutionary phase, which is supported by the SED analysis. Despite the limited sensitivity of the SED analysis to the distinct evolutionary phases, our comprehensive programme of follow-up molecular line observations will be essential to refine the scheme and derive the physical properties of each stage. The results of these follow-up observations will be fully discussed in a number of forthcoming papers (e.g., Navarete et al., in prep.; Giannetti et al., in prep.; Urquhart et al., in prep.).

6. Summary

In this paper we characterize the properties of 110 massive-star forming regions that have been selected to cover important evolutionary stages in the formation of massive stars. This sample includes examples of the coldest pre-stellar stages through to the formation of the ultra-compact H II regions. Using multi-wavelength data, this sample has been classified into four distinct stages: $70\text{ }\mu\text{m}$ weak, mid-infrared weak, mid-infrared bright, and H II regions. Distances for the sources presented in this paper have been revised, incorporating the latest maser parallax measurements.

Exploiting the dust continuum SEDs from mid-infrared to submm wavelengths, we derived dust temperatures and integrated fluxes; these are subsequently used to estimate reliable bolometric luminosities, clump masses, and peak column densities for the whole sample. Comparing the physical properties of the clumps, we found no significant differences between the distances, clump masses, or physical sizes for the different evolutionary phases.

1. The SED analysis provided useful constraints for the dust temperature and integrated emission. We find the dust temperatures to increase from 11 K for the coldest sources to 41 K for the HII regions, with an average value of 24.7 K for the whole sample. A similar trend is seen in the mean bolometric luminosity increasing from $3.2 \times 10^3 L_\odot$ for the $70\text{ }\mu\text{m}$ weak sample to $4.6 \times 10^5 L_\odot$ for the compact HII regions. The classification of the sample is further verified by the continuous increase in the bolometric luminosity to clump mass ratio from an average ratio of 3.4 for the youngest to 86.7 for the most evolved class, all of which is consistent with the proposed evolutionary scheme described in Sect. 2. Although the SED analysis reveals significant differences between the different classes, we also find that there is a large overlap between the different evolutionary phases and additional information is required to confirm and refine the evolutionary scheme.
2. We have found that the majority of the sample satisfy the size-mass criterion for massive-star formation and so have the potential to form massive stars in the future if not already currently doing so. Evaluating the clump stability we find that the vast majority are unstable against gravity and likely to be undergoing global collapse in the absence of significant magnetic support. It therefore seems likely that the majority of the sample will form a cluster that includes at least one massive star. Furthermore, the masses of some clumps exceed $4 \times 10^4 M_\odot$ and have bolometric luminosities in excess of $3 \times 10^6 L_\odot$ and are therefore likely to be forming the most massive, earliest O-type stars.

3. We also give an overview of complementary molecular line observations that are being conducted by the ATLASGAL team to classify the sources in a more robust way. The association rates of methanol and water masers as well as molecular outflows reveals significant differences between the different phases. In addition thermal emission lines and SiO line profiles are used to discriminate the evolutionary stages. Examining a combination of these molecular line and continuum observations, we have found strong support for the proposed evolutionary scheme and verified that the ATLASGAL Top100 sample represents a statistically significant catalog of massive-star forming clumps covering a range of evolutionary phases from the coldest and youngest $70\text{ }\mu\text{m}$ weak to the most evolved clumps hosting H II regions still embedded in their natal environment.

Using well established standard methods we have investigated the full evolutionary sequence from the earliest pre-stellar to the latest embedded H II region phases on a well-selected sample of (almost) exclusively high-mass-star forming clumps drawn from an unbiased dust survey covering the whole inner Galaxy for the first time. Furthermore, as the properties of this sample have been determined in a consistent way and the majority ($\sim 70\%$) is located within 5 kpc these sources are ideal for high resolution follow-up observations to investigate processes such as fragmentation, infall and outflows. This sample therefore provides a solid foundation for more detailed studies to investigate changes of the physical properties and kinematics of the gas through the process of massive-star formation in the future.

Acknowledgements. This work was partially carried out within the Collaborative Research Council 956, sub-project A6, funded by the Deutsche Forschungsgemeinschaft (DFG) and partially funded by the ERC Advanced Investigator Grant GLOSTAR (247078). J. Urquhart and A. Giannetti acknowledge support from the *Deutsche Forschungsgemeinschaft, DFG*, via the Collaborative Research Center (SFB) 956 “Conditions and Impact of Star Formation”. T. Csengeri acknowledges support from the *Deutsche Forschungsgemeinschaft, DFG*, via the SPP (priority programme) 1573 “Physics of the ISM”. This research made use of information from the ATLASGAL database at http://atlasgal.mpifr-bonn.mpg.de/cgi-bin/ATLASGAL_DATABASE.cgi supported by the MPIfR, Bonn, as well as information from the RMS database at http://rms.leeds.ac.uk/cgi-bin/public/RMS_DATABASE.cgi which was constructed with support from the Science and Technology Facilities Council of the UK. This research made use of Astropy⁵, a community-developed core Python package for Astronomy (Astropy Collaboration et al. 2013) and the Astropy affiliate software package photutils⁶. This research made use of Montage, funded by the National Aeronautics and Space Administration’s Earth Science Technology Office, Computation Technologies Project, under Cooperative Agreement Number NCC5-626 between NASA and the California Institute of Technology. Montage is maintained by the NASA/IPAC Infrared Science Archive. This publication also makes use of data products from the Wide-field Infrared Survey Explorer, which is a joint project of the University of California, Los Angeles, and the Jet Propulsion Laboratory/California Institute of Technology, funded by the National Aeronautics and Space Administration.

References

- Aguirre, J. E., Ginsburg, A. G., Dunham, M. K., et al. 2011, *ApJS*, **192**, 4
 Astropy Collaboration, Robitaille, T. P., Tollerud, E. J., et al. 2013, *A&A*, **558**, A33
 Bacmann, A., Lefloch, B., Ceccarelli, C., et al. 2002, *A&A*, **389**, L6
 Benjamin, R. A., Churchwell, E., Babler, B. L., et al. 2003, *PASP*, **115**, 953
 Bernard, J.-P., Paradis, D., Marshall, D. J., et al. 2010, *A&A*, **518**, L88
 Bertoldi, F., & McKee, C. F. 1992, *ApJ*, **395**, 140
 Beuther, H., Henning, T., Linz, H., et al. 2010, *A&A*, **518**, L78
 Bonnor, W. B. 1955, *MNRAS*, **115**, 310
 Breen, S. L., Fuller, G. A., Caswell, J. L., et al. 2015, *MNRAS*, **450**, 4109
 Brunthaler, A., Reid, M. J., Menten, K. M., et al. 2009, *ApJ*, **693**, 424
 Busfield, A. L., Purcell, C. R., Hoare, M. G., et al. 2006, *MNRAS*, **366**, 1096
 Carey, S. J., Noriega-Crespo, A., Mizuno, D. R., et al. 2009, *PASP*, **121**, 76
 Caselli, P., Walmsley, C. M., Terzieva, R., & Herbst, E. 1998, *ApJ*, **499**, 234
 Caswell, J. L., Murray, J. D., Roger, R. S., Cole, D. J., & Cooke, D. J. 1975, *A&A*, **45**, 239
 Churchwell, E., Babler, B. L., Meade, M. R., et al. 2009, *PASP*, **121**, 213
 Contreras, Y., Schuller, F., Urquhart, J. S., et al. 2013, *A&A*, **549**, A45
 Crutcher, R. M. 2012, *ARA&A*, **50**, 29
 Csengeri, T., Urquhart, J. S., Schuller, F., et al. 2014, *A&A*, **565**, A75
 Csengeri, T., Leurini, S., Wyrowski, F., et al. 2016, *A&A*, **586**, A149
 Cutri, R. M., Wright, E. L., Conrow, T., et al. 2012, Explanatory Supplement to the WISE All-Sky Data Release Products, Tech. Rep.
 Davies, B., Clark, J. S., Trombley, C., et al. 2012, *MNRAS*, **419**, 1871
 de Villiers, H. M., Chrysostomou, A., Thompson, M. A., et al. 2014, *MNRAS*, **444**, 566
 de Villiers, H. M., Chrysostomou, A., Thompson, M. A., et al. 2015, *MNRAS*, **449**, 119
 de Wit, W. J., Testi, L., Palla, F., Vanzi, L., & Zinnecker, H. 2004, *A&A*, **425**, 937
 Egan, M. P., Price, S. D., Kraemer, K. E., et al. 2003, *VizieR Online Data Catalog*: V/114
 Elia, D., & Pezzuto, S. 2016, *MNRAS*, **461**, 1328
 Elia, D., Schisano, E., Molinari, S., et al. 2010, *A&A*, **518**, L97
 Elia, D., Molinari, S., Fukui, Y., et al. 2013, *ApJ*, **772**, 45
 Feng, S., Beuther, H., Zhang, Q., et al. 2016, *ApJ*, **828**, 100
 Gallaway, M., Thompson, M. A., Lucas, P. W., et al. 2013, *MNRAS*, **430**, 808
 Giannetti, A., Wyrowski, F., Brand, J., et al. 2014, *A&A*, **570**, A65
 Giannetti, A., Wyrowski, F., Leurini, S., et al. 2015, *A&A*, **580**, L7
 Green, J. A., & McClure-Griffiths, N. M. 2011, *MNRAS*, **417**, 2500
 Griffin, M. J., Abergel, A., Abreu, A., et al. 2010, *A&A*, **518**, L3
 Güsten, R., Nyman, L. Å., Schilke, P., et al. 2006, *A&A*, **454**, L13
 Gutermuth, R. A., & Heyer, M. 2015, *AJ*, **149**, 64
 Heyer, M., Gutermuth, R., Urquhart, J. S., et al. 2016, *A&A*, **588**, A29
 Hildebrand, R. H. 1983, *QJRAS*, **24**, 267
 Hoare, M. G., Purcell, C. R., Churchwell, E. B., et al. 2012, *PASP*, **124**, 939
 Immer, K., Schuller, F., Omont, A., & Menten, K. M. 2012, *A&A*, **537**, A121
 Immer, K., Reid, M. J., Menten, K. M., Brunthaler, A., & Dame, T. M. 2013, *A&A*, **553**, A117
 Kauffmann, J., Bertoldi, F., Bourke, T. L., Evans, II, N. J., & Lee, C. W. 2008, *A&A*, **487**, 993
 Kauffmann, J., Pillai, T., Shetty, R., Myers, P. C., & Goodman, A. A. 2010, *ApJ*, **712**, 1137
 Kauffmann, J., Pillai, T., & Goldsmith, P. F. 2013, *ApJ*, **779**, 185
 Kennicutt, R. C. 2005, in Massive Star Birth: A Crossroads of Astrophysics, eds. R. Cesaroni, M. Felli, E. Churchwell, & M. Walmsley, *IAU Symp.*, **227**, 3
 Kurayama, T., Nakagawa, A., Sawada-Satoh, S., et al. 2011, *PASJ*, **63**, 513
 Lucas, P. W., Hoare, M. G., Longmore, A., et al. 2008, *MNRAS*, **391**, 136
 Moisés, A. P., Damineli, A., Figueiredo, E., et al. 2011, *MNRAS*, **411**, 705
 Molinari, S., Pezzuto, S., Cesaroni, R., et al. 2008, *A&A*, **481**, 345
 Molinari, S., Swinyard, B., Bally, J., et al. 2010, *PASP*, **122**, 314
 Molinari, S., Schisano, E., Elia, D., et al. 2016, *A&A*, **591**, A149
 Motte, F., Zavagno, A., Bontemps, S., et al. 2010, *A&A*, **518**, L77
 Mottram, J. C., Hoare, M. G., Davies, B., et al. 2011a, *ApJ*, **730**, L33
 Mottram, J. C., Hoare, M. G., Urquhart, J. S., et al. 2011b, *A&A*, **525**, A149
 Nguyen Luong, Q., Motte, F., Hennemann, M., et al. 2011, *A&A*, **535**, A76
 Ossenkopf, V., & Henning, T. 1994, *A&A*, **291**, 943
 Pilbratt, G. L., Riedinger, J. R., Passvogel, T., et al. 2010, *A&A*, **518**, L1
 Pillai, T. 2016, in *EAS Pub. Ser.*, **75**, 245
 Poglitsch, A., Waelkens, C., Geis, N., et al. 2010, *A&A*, **518**, L2
 Price, S. D., Egan, M. P., Carey, S. J., Mizuno, D. R., & Kuchar, T. A. 2001, *AJ*, **121**, 2819
 Purcell, C. R., Hoare, M. G., Cotton, W. D., et al. 2013, *ApJS*, **205**, 1
 Razali, N. M., & Wah, Y. B. 2011, *J. Stat. Modeling and Analytics*, **2**, 21
 Reid, M. J., Menten, K. M., Brunthaler, A., et al. 2014, *ApJ*, **783**, 130
 Robitaille, T. P., Whitney, B. A., Indebetouw, R., & Wood, K. 2007, *ApJS*, **169**, 328
 Roman-Duval, J., Jackson, J. M., Heyer, M., et al. 2009, *ApJ*, **699**, 1153
 Sanna, A., Reid, M. J., Menten, K. M., et al. 2014, *ApJ*, **781**, 108
 Sato, M., Reid, M. J., Brunthaler, A., & Menten, K. M. 2010, *ApJ*, **720**, 1055
 Sato, M., Wu, Y. W., Immer, K., et al. 2014, *ApJ*, **793**, 72
 Schuller, F., Menten, K. M., Contreras, Y., Wyrowski, F., & Schilke, E. A. 2009, *A&A*, **504**, 415
 Siringo, G., Kreysa, E., Kovács, A., et al. 2009, *A&A*, **497**, 945
 Snell, R. L., Dickman, R. L., & Huang, Y.-L. 1990, *ApJ*, **352**, 139
 Sridharan, T. K., Beuther, H., Schilke, P., Menten, K. M., & Wyrowski, F. 2002, *ApJ*, **566**, 931
 Stephens, M. A. 1974, *J. Am. Stat. Assoc.*, **69**, 730
 Tan, J. C., Kong, S., Zhang, Y., et al. 2016, *ApJ*, **821**, L3

⁵ <http://www.astropy.org>

⁶ <https://github.com/astropy/photutils>

- Thompson, M. A., White, G. J., Morgan, L. K., et al. 2004, [A&A](#), **414**, 1017
- Traficante, A., Fuller, G. A., Peretto, N., Pineda, J. E., & Molinari, S. 2015, [MNRAS](#), **451**, 3089
- Urban, A., Evans, II, N. J., & Doty, S. D. 2009, [ApJ](#), **698**, 1341
- Urquhart, J. S., Busfield, A. L., Hoare, M. G., et al. 2007, [A&A](#), **461**, 11
- Urquhart, J. S., Morgan, L. K., & Thompson, M. A. 2009, [A&A](#), **497**, 789
- Urquhart, J. S., Hoare, M. G., Lumsden, S. L., et al. 2012, [MNRAS](#), **420**, 1656
- Urquhart, J. S., Moore, T. J. T., Schuller, F., et al. 2013a, [MNRAS](#), **431**, 1752
- Urquhart, J. S., Thompson, M. A., Moore, T. J. T., et al. 2013b, [MNRAS](#), **435**, 400
- Urquhart, J. S., Csengeri, T., Wyrowski, F., et al. 2014a, [A&A](#), **568**, A41
- Urquhart, J. S., Figura, C. C., Moore, T. J. T., et al. 2014b, [MNRAS](#), **437**, 1791
- Urquhart, J. S., Moore, T. J. T., Csengeri, T., et al. 2014c, [MNRAS](#), **443**, 1555
- Urquhart, J. S., Moore, T. J. T., Menten, K. M., et al. 2015, [MNRAS](#), **446**, 3461
- Walsh, A. J., Hyland, A. R., Robinson, G., & Burton, M. G. 1997, [MNRAS](#), **291**, 261
- Walsh, A. J., Burton, M. G., Hyland, A. R., & Robinson, G. 1998, [MNRAS](#), **301**, 640
- Walsh, A. J., Macdonald, G. H., Alvey, N. D. S., Burton, M. G., & Lee, J.-K. 2003, [A&A](#), **410**, 597
- Walsh, A. J., Breen, S. L., Britton, T., et al. 2011, in EAS Pub. Ser., 52, eds. M. Röllig, R. Simon, V. Ossenkopf, & J. Stutzki, 135
- Walsh, A. J., Purcell, C. R., Longmore, S. N., et al. 2014, [MNRAS](#), **442**, 2240
- Whitney, B. A., Robitaille, T. P., Wood, K., Denzmore, P., & Bjorkman, J. E. 2005, in *Protostars and Planets V*. Proc. Conf., **1286**, 8460
- Wienen, M., Wyrowski, F., Menten, K. M., et al. 2015, [A&A](#), **579**, A91
- Wood, D. O. S., & Churchwell, E. 1989, [ApJS](#), **69**, 831
- Wright, E. L., Eisenhardt, P. R. M., Mainzer, A. K., et al. 2010, [AJ](#), **140**, 1868
- Wu, Y. W., Sato, M., Reid, M. J., et al. 2014, [A&A](#), **566**, A17
- Wyrowski, F., Güsten, R., Menten, K. M., et al. 2016, [A&A](#), **585**, A149
- Xu, Y., Reid, M. J., Menten, K. M., et al. 2009, [ApJ](#), **693**, 413
- Xu, Y., Moscadelli, L., Reid, M. J., et al. 2011, [ApJ](#), **733**, 25
- Zhang, B., Zheng, X. W., Reid, M. J., et al. 2009, [ApJ](#), **693**, 419
- Zhang, B., Reid, M. J., Menten, K. M., et al. 2013, [ApJ](#), **775**, 79
- Zhang, B., Moscadelli, L., Sato, M., et al. 2014, [ApJ](#), **781**, 89
- Zinnecker, H., & Yorke, H. W. 2007, [ARA&A](#), **45**, 481

Appendix A: Full data

Table A.1. Source parameters.

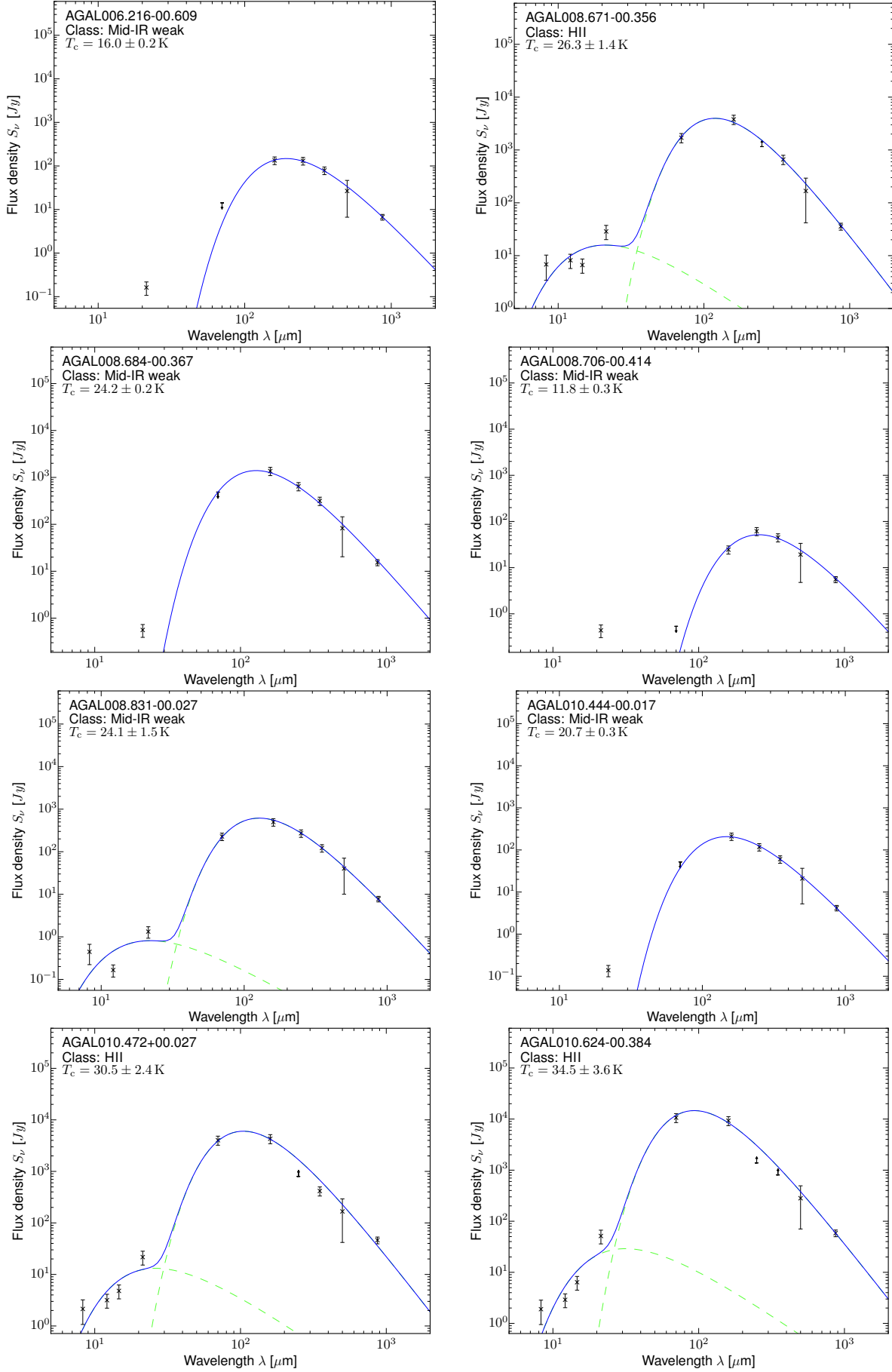
Name	d (kpc)	d_{ref}	V_{LSR} (km s $^{-1}$)	l_{app} (deg)	b_{app} (deg)	D_{app} (‘‘)	Class	T (K)	ΔT (K)	L_{bol} (L_{\odot})	M_{clump} (M_{\odot})	α_{vir}
AGAL006.216–00.609	2.9	(22)	18.5	6.216	-0.609	71.6	IRw	16.0	0.2	7.3×10^2	4.5×10^2	–
AGAL008.671–00.356	4.8	(19)	35.1	8.668	-0.355	69.1	HII	26.3	1.4	8.6×10^4	3.0×10^3	–
AGAL008.684–00.367	4.8	(19)	38.0	8.682	-0.367	66.1	IRw	24.2	0.2	2.7×10^4	1.4×10^3	0.69
AGAL008.706–00.414	4.8	(19)	39.4	8.704	-0.412	92.1	IRw	11.8	0.3	5.0×10^2	1.6×10^3	0.22
AGAL008.831–00.027	–	–	0.5	8.831	-0.027	70.9	IRw	24.1	1.5	–	–	–
AGAL010.444–00.017	8.6	(1)	75.9	10.442	-0.016	65.5	IRw	20.7	0.3	1.1×10^4	1.6×10^3	0.40
AGAL010.472+00.027	8.6	(1)	67.6	10.472	+0.028	55.1	HII	30.5	2.4	4.6×10^5	1.0×10^4	0.22
AGAL010.624–00.384	5.0	(1)	-2.9	10.623	-0.382	65.0	HII	34.5	3.6	4.2×10^5	3.7×10^3	0.42
AGAL012.804–00.199	2.4	(28)	36.2	12.805	-0.197	84.4	HII	35.1	2.3	2.4×10^5	1.8×10^3	0.78
AGAL013.178+00.059	2.4	(25)	50.4	13.176	+0.062	87.6	70w	24.2	0.8	8.3×10^3	3.6×10^2	0.96
AGAL013.658–00.599	4.5	(22)	48.4	13.656	-0.596	67.0	IRb	27.4	1.3	2.0×10^4	5.6×10^2	0.53
AGAL014.114–00.574	2.6	(3)	20.8	14.112	-0.572	81.0	IRw	22.4	0.8	3.1×10^3	3.5×10^2	0.65
AGAL014.194–00.194	3.9	(3)	39.2	14.194	-0.191	72.0	IRw	18.2	0.6	2.7×10^3	8.2×10^2	0.50
AGAL014.492–00.139	3.9	(3)	39.5	14.491	-0.137	89.3	70w	12.4	0.4	7.5×10^2	1.9×10^3	0.55
AGAL014.632–00.577	1.8	(27)	18.5	14.631	-0.576	83.5	IRw	22.5	0.4	2.7×10^3	2.5×10^2	0.84
AGAL015.029–00.669	2.0	(9)	19.6	15.032	-0.674	98.6	IRb	32.9	1.5	1.3×10^5	1.1×10^3	0.19
AGAL018.606–00.074	4.3	(7)	46.6	18.606	-0.074	74.8	IRw	13.8	0.3	5.9×10^2	8.7×10^2	0.46
AGAL018.734–00.226	12.5	(19)	42.6	18.734	-0.224	74.1	IRw	21.9	1.0	7.2×10^4	7.9×10^3	0.45
AGAL018.888–00.474	4.7	(19)	66.1	18.888	-0.472	81.5	IRw	14.4	0.2	3.2×10^3	2.8×10^3	0.54
AGAL019.609–00.234	12.6	(22)	40.8	19.608	-0.233	60.1	HII	32.4	1.2	1.1×10^6	1.3×10^4	–
AGAL019.882–00.534	3.7	(19)	45.0	19.882	-0.532	66.7	IRb	24.2	1.4	1.2×10^4	7.9×10^2	0.41
AGAL022.376+00.447	4.0	(19)	54.0	22.376	+0.447	64.7	IRw	13.1	0.4	3.1×10^2	6.2×10^2	0.10
AGAL023.206–00.377	4.6	(5)	78.2	23.206	-0.377	60.7	IRw	22.1	0.1	1.2×10^4	1.2×10^3	0.44
AGAL024.416+00.101	7.7	(17)	112.2	24.418	+0.102	84.5	IRw	15.4	0.2	4.2×10^3	2.4×10^3	–
AGAL024.629+00.172	7.7	(17)	116.0	24.631	+0.174	72.0	IRw	18.1	0.5	5.0×10^3	1.5×10^3	0.85
AGAL024.651–00.169	7.7	(17)	113.0	24.653	-0.169	86.5	70w	18.6	1.0	6.8×10^3	1.8×10^3	–
AGAL024.789+00.082	7.7	(17)	110.2	24.789	+0.085	69.0	HII	26.5	2.5	1.9×10^5	6.8×10^3	–
AGAL028.564–00.236	5.5	(3)	87.2	28.566	-0.232	101.3	IRw	11.7	0.1	1.7×10^3	5.4×10^3	0.40
AGAL028.861+00.066	7.4	(8)	104.0	28.861	+0.067	69.1	IRb	34.5	1.7	1.6×10^5	1.0×10^3	0.39
AGAL030.818–00.056	4.9	(2)	97.8	30.816	-0.055	65.3	IRb	22.9	0.1	6.3×10^4	5.6×10^3	0.28
AGAL030.848–00.081	4.9	(2)	94.4	30.848	-0.082	78.4	70w	16.7	0.2	3.1×10^3	1.2×10^3	0.10
AGAL030.893+00.139	4.9	(2)	97.3	30.893	+0.139	84.7	70w	11.4	0.5	4.9×10^2	1.9×10^3	0.41
AGAL031.412+00.307	4.9	(2)	98.2	31.411	+0.308	58.9	HII	26.3	1.8	6.8×10^4	3.0×10^3	0.31
AGAL034.258+00.154	1.6	(20)	58.5	34.256	+0.155	66.5	HII	31.0	1.2	4.8×10^4	8.0×10^2	0.57
AGAL034.401+00.226	1.6	(20)	57.4	34.402	+0.229	81.5	HII	22.8	1.2	2.9×10^3	2.7×10^2	1.94
AGAL034.411+00.234	1.6	(20)	58.0	34.411	+0.236	62.6	IRb	26.1	1.8	4.8×10^3	2.1×10^2	1.20
AGAL034.821+00.351	1.6	(20)	58.3	34.819	+0.351	89.0	IRb	24.7	0.6	2.7×10^3	1.1×10^2	1.62
AGAL035.197–00.742	2.2	(21)	34.7	35.197	-0.743	73.5	IRb	29.5	2.7	2.3×10^4	4.6×10^2	0.90
AGAL035.579+00.007	10.3	(22)	53.1	35.576	+0.011	109.8	70w	14.5	0.2	9.1×10^3	1.0×10^4	–
AGAL037.554+00.201	6.7	(17)	86.1	37.552	+0.201	69.5	IRb	28.4	1.8	5.1×10^4	1.2×10^3	0.67
AGAL043.166+00.011	11.1	(4)	5.3	43.165	+0.012	68.5	HII	34.0	2.7	3.7×10^6	4.3×10^4	0.08
AGAL049.489–00.389	5.4	(10)	57.2	49.488	-0.388	62.1	HII	29.1	1.2	5.5×10^5	1.1×10^4	0.18
AGAL053.141+00.069	1.6	(18)	22.3	53.141	+0.071	66.8	IRb	25.4	0.7	2.3×10^3	9.4×10^1	1.59
AGAL059.782+00.066	2.2	(24)	23.1	59.782	+0.066	78.9	IRb	28.2	1.5	9.7×10^3	2.5×10^2	0.71
AGAL301.136–00.226	4.4	(19)	-39.2	301.136	-0.224	62.1	HII	34.6	2.8	2.1×10^5	1.9×10^3	0.42
AGAL305.192–00.006	3.8	(16)	-34.2	305.192	-0.004	73.7	IRw	26.1	3.1	1.2×10^4	5.1×10^2	0.96
AGAL305.209+00.206	3.8	(16)	-42.5	305.208	+0.208	68.0	IRb	30.1	0.9	8.8×10^4	1.4×10^3	0.73
AGAL305.562+00.014	3.8	(16)	-39.8	305.561	+0.014	67.9	IRb	33.4	1.9	5.1×10^4	4.0×10^2	1.00
AGAL305.794–00.096	3.8	(16)	-40.8	305.794	-0.096	84.7	70w	16.0	0.1	9.8×10^2	5.9×10^2	0.62

Notes. The Columns are as follows: Name: the ATLASGAL catalog source name; d : distance; d_{ref} : distance reference (see list of references below table); V_{lsr} : source velocity; l_{app} : Galactic longitude of aperture center; b_{app} : Galactic latitude of aperture center; D_{app} : aperture diameter; Class: class of the source (HII: HII region, IRb: mid-infrared bright, 2d: mid-infrared weak (c: confused within the aperture), 70d: 70 μm weak); T : dust temperature; ΔT : Error of the dust temperature; L_{bol} : bolometric luminosity; M_{clump} : clump mass; α_{vir} : virial parameter.

References. Distance references: (1): Sanna et al. (2014); (2): Zhang et al. (2014); (3): Giannetti et al. (2014); (4): Zhang et al. (2013); (5): Brunthaler et al. (2009); (6): Giannetti et al. (2015); (7): Kurayama et al. (2011); (8): Sato et al. (2014); (9): Xu et al. (2011); (10): Sato et al. (2010); (11): Urquhart et al. (2012); (13): Moisés et al. (2011); (14): Busfield et al. (2006); (15): Snell et al. (1990); (16): Davies et al. (2012); (17): Tangent Point; (18): Roman-Duval et al. (2009); (19): Green & McClure-Griffiths (2011); (20): Zhang et al. (2009); (21): Wienen et al. (2015); (22): Urquhart et al. (2014b); (23): Xu et al. (2009); (24): Immer et al. (2013); (25): Caswell et al. (1975); (26): Wu et al. (2014); (27): Immer et al. (2012).

Table A.1. continued.

Name	d (kpc)	d_{ref}	V_{LSR} (km s $^{-1}$)	l_{app} (deg)	b_{app} (deg)	D_{app} (")	Class	T (K)	ΔT (K)	L_{bol} (L_{\odot})	M_{clump} (M_{\odot})	α_{vir}
AGAL309.384–00.134	5.3	(19)	−51.3	309.383	−0.134	74.9	IRb	24.0	1.3	1.5×10^4	1.2×10^3	0.65
AGAL310.014+00.387	3.6	(3)	−41.3	310.011	+0.389	76.6	IRb	32.2	1.1	4.9×10^4	4.1×10^2	1.14
AGAL313.576+00.324	3.8	(19)	−46.9	313.576	+0.326	57.8	IRb	29.2	1.8	9.4×10^3	1.8×10^2	1.68
AGAL316.641–00.087	1.2	(23)	−17.7	316.639	−0.086	62.2	IRb	30.6	1.9	9.9×10^2	1.8×10^1	5.44
AGAL317.867–00.151	3.0	(3)	−40.2	317.867	−0.149	62.3	IRw	19.3	0.5	1.6×10^3	3.6×10^2	0.94
AGAL318.779–00.137	2.8	(3)	−38.1	318.778	−0.136	86.5	IRw	24.9	1.5	6.3×10^3	3.5×10^2	1.45
AGAL320.881–00.397	10.0	(3)	−45.3	320.879	−0.396	69.1	70w	16.8	0.2	6.0×10^3	2.8×10^3	0.20
AGAL326.661+00.519	1.8	(13)	−39.8	326.661	+0.521	74.2	IRb	28.4	0.8	7.4×10^3	1.2×10^2	1.25
AGAL326.987–00.032	4.0	(3)	−58.6	326.986	−0.029	63.7	IRw	17.9	2.4	1.1×10^3	4.4×10^2	1.80
AGAL327.119+00.509	5.5	(19)	−83.6	327.119	+0.511	67.7	IRb	31.8	1.2	5.8×10^4	6.7×10^2	0.71
AGAL327.293–00.579	3.1	(22)	−44.7	327.291	−0.578	58.8	IRb	27.9	2.2	8.3×10^4	2.8×10^3	0.29
AGAL327.393+00.199	5.9	(19)	−89.2	327.391	+0.201	70.1	IRb	23.2	1.0	1.3×10^4	1.1×10^3	0.53
AGAL328.809+00.632	3.0	(19)	−41.9	328.808	+0.635	64.7	HII	36.3	3.2	1.5×10^5	1.0×10^3	0.70
AGAL329.029–00.206	11.5	(19)	−43.5	329.029	−0.197	89.3	IRw	23.1	0.6	2.1×10^5	1.1×10^4	0.16
AGAL329.066–00.307	11.6	(19)	−41.9	329.064	−0.306	87.4	IRb	21.9	1.0	7.1×10^4	9.0×10^3	0.33
AGAL330.879–00.367	4.2	(26)	−62.5	330.878	−0.366	63.0	HII	33.4	3.0	1.5×10^5	1.5×10^3	0.48
AGAL330.954–00.182	9.3	(11)	−91.2	330.952	−0.181	58.6	HII	33.0	4.5	1.3×10^6	1.7×10^4	0.25
AGAL331.709+00.582	10.5	(3)	−67.8	331.707	+0.584	72.2	IRw	21.0	0.3	3.7×10^4	5.1×10^3	0.53
AGAL332.094–00.421	3.6	(13)	−56.9	332.094	−0.419	70.0	IRb	30.8	0.7	5.8×10^4	6.2×10^2	0.86
AGAL332.826–00.549	3.6	(13)	−57.1	332.824	−0.549	63.6	HII	35.7	2.8	2.4×10^5	1.9×10^3	0.51
AGAL333.134–00.431	3.6	(13)	−53.1	333.133	−0.43	77.4	HII	35.2	1.7	4.1×10^5	2.8×10^3	0.89
AGAL333.284–00.387	3.6	(13)	−52.4	333.284	−0.387	85.4	HII	30.4	1.8	1.2×10^5	2.0×10^3	0.41
AGAL333.314+00.106	3.6	(13)	−46.5	333.314	+0.106	70.6	IRb	25.9	1.5	1.0×10^4	4.2×10^2	1.63
AGAL333.604–00.212	3.6	(13)	−48.4	333.602	−0.21	85.2	HII	41.1	2.4	1.2×10^6	3.4×10^3	0.77
AGAL333.656+00.059	5.3	(3)	−85.0	333.656	+0.059	84.7	70w	17.8	0.3	4.2×10^3	1.4×10^3	0.53
AGAL335.789+00.174	3.7	(19)	−50.1	335.789	+0.176	71.7	IRw	24.7	0.9	2.0×10^4	1.1×10^3	0.46
AGAL336.958–00.224	10.9	(19)	−71.3	336.956	−0.224	57.8	IRw	15.8	1.0	3.6×10^3	2.4×10^3	0.11
AGAL337.176–00.032	11.0	(6)	−67.8	337.174	−0.031	82.6	IRw	22.3	1.2	5.9×10^4	5.5×10^3	0.17
AGAL337.258–00.101	11.0	(6)	−68.3	337.258	−0.099	68.0	IRw	21.7	0.9	3.0×10^4	3.1×10^3	0.33
AGAL337.286+00.007	9.4	(3)	−106.6	337.284	+0.009	86.7	70w	10.7	0.5	1.2×10^3	6.6×10^3	0.09
AGAL337.406–00.402	3.3	(19)	−41.0	337.404	−0.402	66.3	HII	31.8	2.3	8.5×10^4	1.1×10^3	0.55
AGAL337.704–00.054	12.3	(19)	−47.4	337.704	−0.053	63.7	HII	25.6	0.6	3.1×10^5	1.4×10^4	0.28
AGAL337.916–00.477	3.2	(26)	−39.6	337.914	−0.476	61.9	IRb	34.4	1.8	1.2×10^5	1.2×10^3	0.45
AGAL338.066+00.044	4.7	(3)	−69.2	338.066	+0.046	89.2	70w	18.5	1.4	3.1×10^3	9.6×10^2	2.86
AGAL338.786+00.476	4.5	(3)	−63.8	338.782	+0.477	84.8	70w	12.2	0.6	4.8×10^2	1.2×10^3	0.38
AGAL338.926+00.554	4.4	(19)	−61.6	338.924	+0.558	89.9	IRb	24.2	1.0	9.4×10^4	5.9×10^3	0.43
AGAL339.623–00.122	3.0	(19)	−34.6	339.621	−0.121	80.2	IRb	28.7	1.4	1.4×10^4	3.1×10^2	1.16
AGAL340.374–00.391	3.6	(3)	−43.6	340.372	−0.389	72.2	IRw	13.4	0.1	5.1×10^2	7.9×10^2	0.49
AGAL340.746–01.001	2.8	(3)	−29.4	340.744	−1.001	75.1	IRb	27.1	0.3	7.6×10^3	2.1×10^2	1.55
AGAL340.784–00.097	10.0	(19)	−101.5	340.784	−0.096	61.4	IRw	26.2	0.4	7.2×10^4	2.8×10^3	0.45
AGAL341.217–00.212	3.7	(19)	−43.6	341.216	−0.211	65.6	IRb	27.0	1.3	1.6×10^4	4.8×10^2	0.74
AGAL342.484+00.182	12.6	(19)	−41.5	342.483	+0.182	64.8	IRw	23.6	0.7	6.4×10^4	4.9×10^3	0.12
AGAL343.128–00.062	3.0	(3)	−30.6	343.125	−0.062	69.1	HII	30.9	4.5	7.1×10^4	1.1×10^3	0.69
AGAL343.756–00.164	2.9	(14)	−27.8	343.756	−0.162	60.9	IRw	24.3	1.4	9.8×10^3	6.1×10^2	0.43
AGAL344.227–00.569	2.5	(19)	−22.3	344.225	−0.569	63.0	IRw	22.0	1.3	9.7×10^3	1.1×10^3	0.35
AGAL345.003–00.224	3.0	(19)	−27.6	345.002	−0.222	65.2	HII	31.0	2.8	6.4×10^4	9.6×10^2	0.79
AGAL345.488+00.314	2.2	(19)	−17.6	345.487	+0.316	86.3	HII	30.7	1.7	6.1×10^4	9.2×10^2	0.95
AGAL345.504+00.347	2.2	(26)	−17.8	345.504	+0.35	75.2	IRb	32.7	1.5	4.3×10^4	4.2×10^2	1.70
AGAL345.718+00.817	1.6	(3)	−11.2	345.716	+0.817	94.9	IRb	22.1	1.3	1.8×10^3	2.0×10^2	0.67
AGAL351.131+00.771	1.8	(13)	−5.3	351.133	+0.771	80.5	70w	18.6	0.3	6.2×10^2	1.2×10^2	0.76
AGAL351.161+00.697	1.8	(13)	−6.7	351.16	+0.698	76.4	IRb	21.9	3.4	8.7×10^3	1.1×10^3	0.46
AGAL351.244+00.669	1.8	(13)	−3.3	351.245	+0.67	99.0	IRb	32.5	2.2	7.7×10^4	8.8×10^2	0.46
AGAL351.416+00.646	1.3	(27)	−7.4	351.416	+0.645	59.6	HII	33.4	1.5	3.9×10^4	4.6×10^2	0.54
AGAL351.444+00.659	1.3	(27)	−4.3	351.444	+0.659	94.4	IRw	21.4	1.1	9.5×10^3	1.4×10^3	0.28
AGAL351.571+00.762	1.3	(27)	−3.2	351.569	+0.762	107.8	70w	17.0	0.1	4.3×10^2	1.6×10^2	0.64
AGAL351.581–00.352	6.8	(19)	−95.9	351.581	−0.352	65.6	IRb	27.1	2.6	2.4×10^5	8.7×10^3	0.13
AGAL351.774–00.537	1.0	(15)	−2.8	351.775	−0.535	63.3	IRb	31.8	3.5	1.6×10^4	2.6×10^2	1.05
AGAL353.066+00.452	0.9	(22)	1.7	353.066	+0.452	72.1	IRw	17.8	0.2	5.7×10^1	1.7×10^1	2.27
AGAL353.409–00.361	3.4	(22)	−16.0	353.408	−0.359	90.4	IRb	28.3	1.7	1.2×10^5	3.4×10^3	0.27
AGAL353.417–00.079	6.1	(3)	−54.4	353.416	−0.079	93.7	70w	17.1	0.4	4.5×10^3	1.7×10^3	0.11
AGAL354.944–00.537	1.9	(3)	−5.4	354.944	−0.537	88.2	70w	19.1	1.3	4.8×10^2	1.4×10^2	1.13

**Fig. A.1.** Source SEDs.

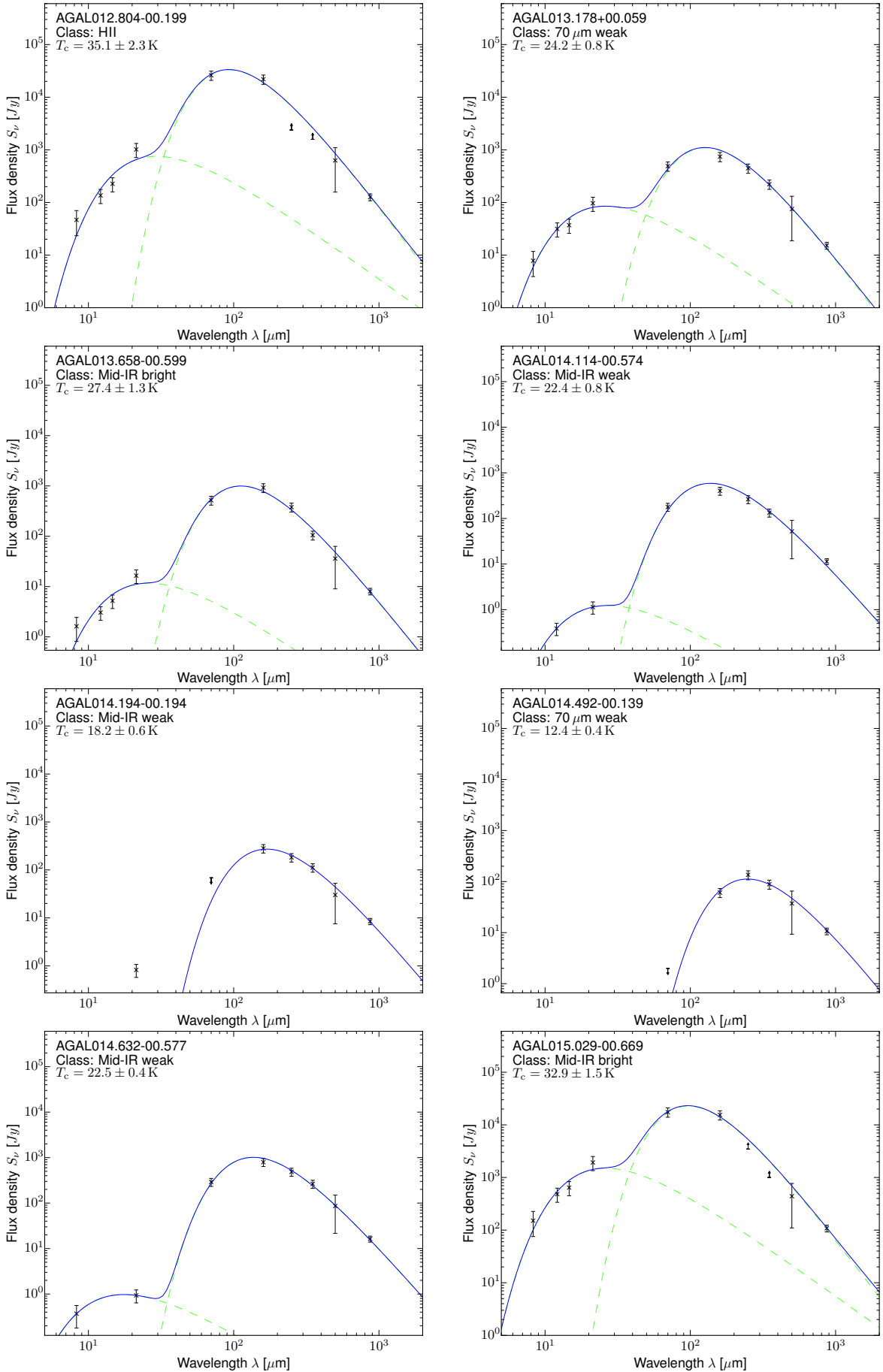
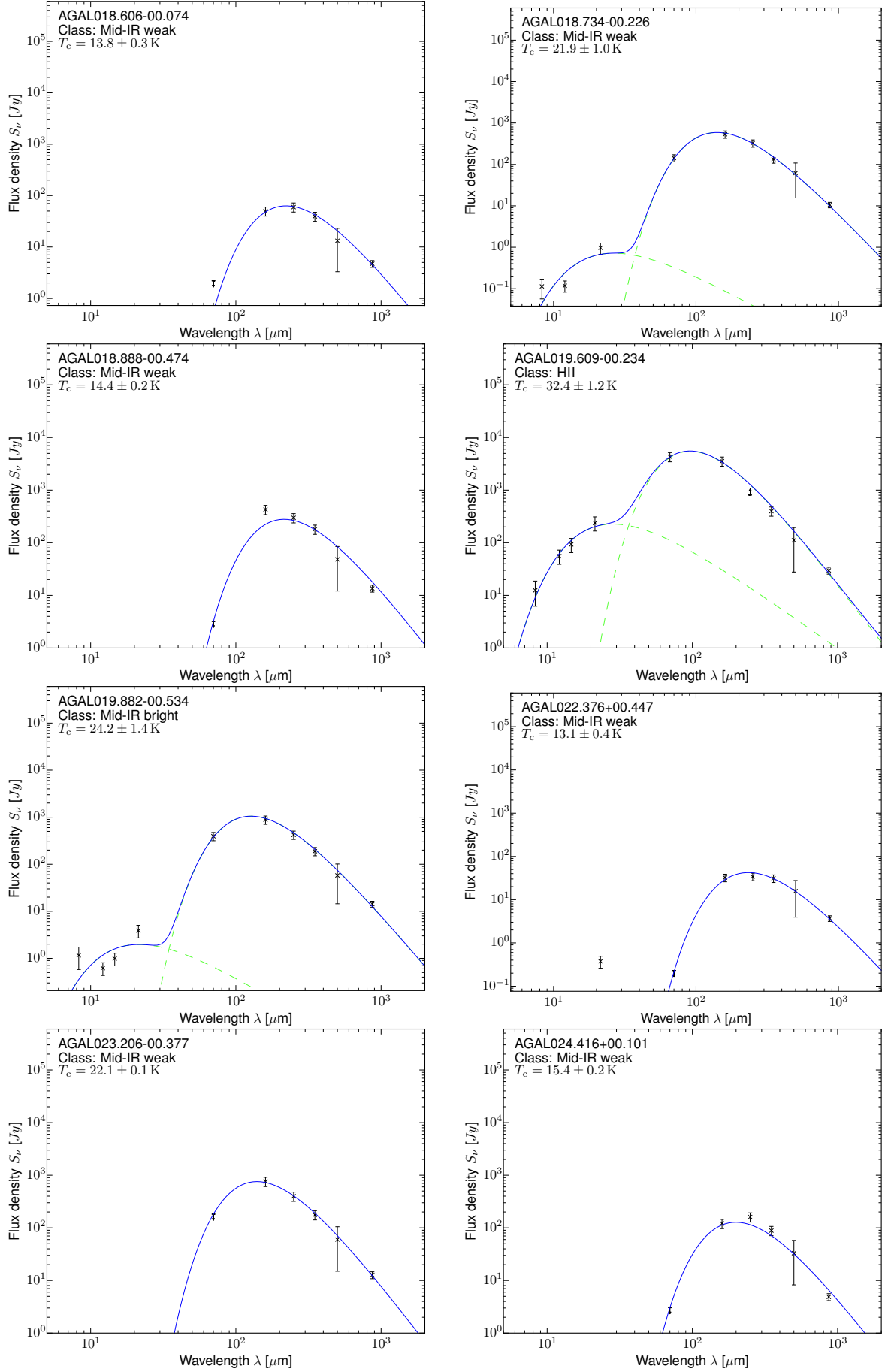


Fig. A.1. continued.

**Fig. A.1.** continued.

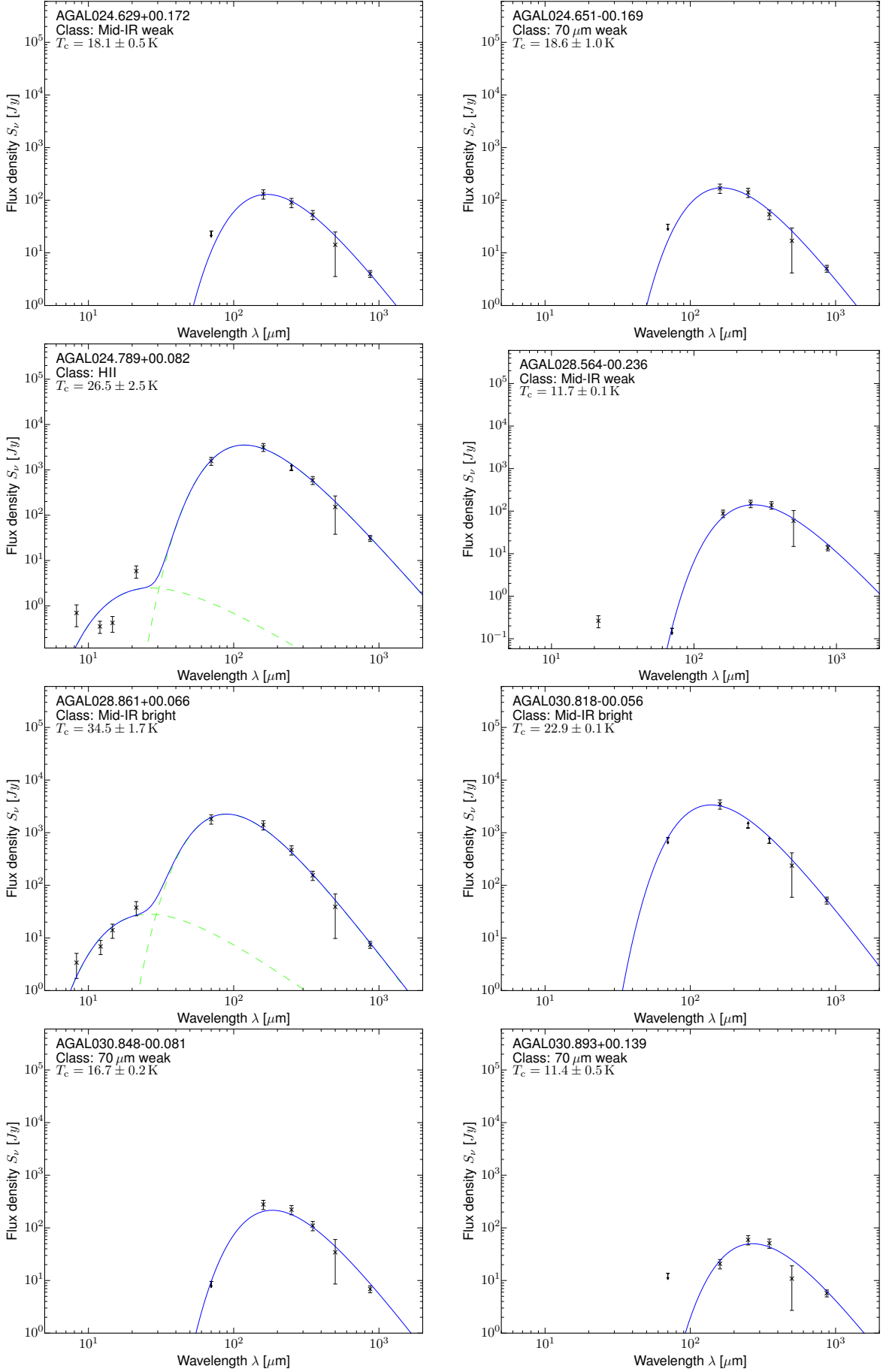
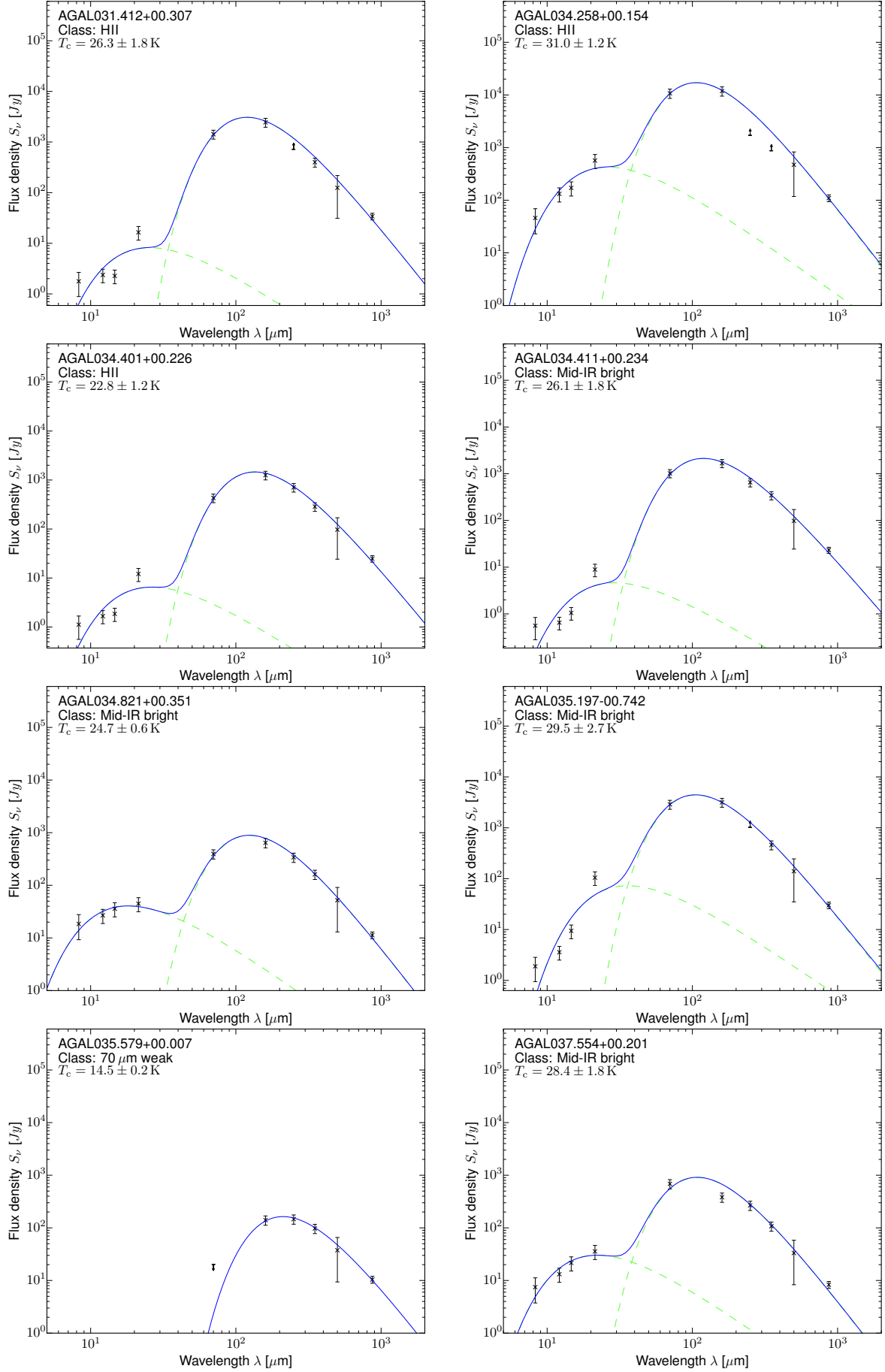


Fig. A.1. continued.

**Fig. A.1.** continued.

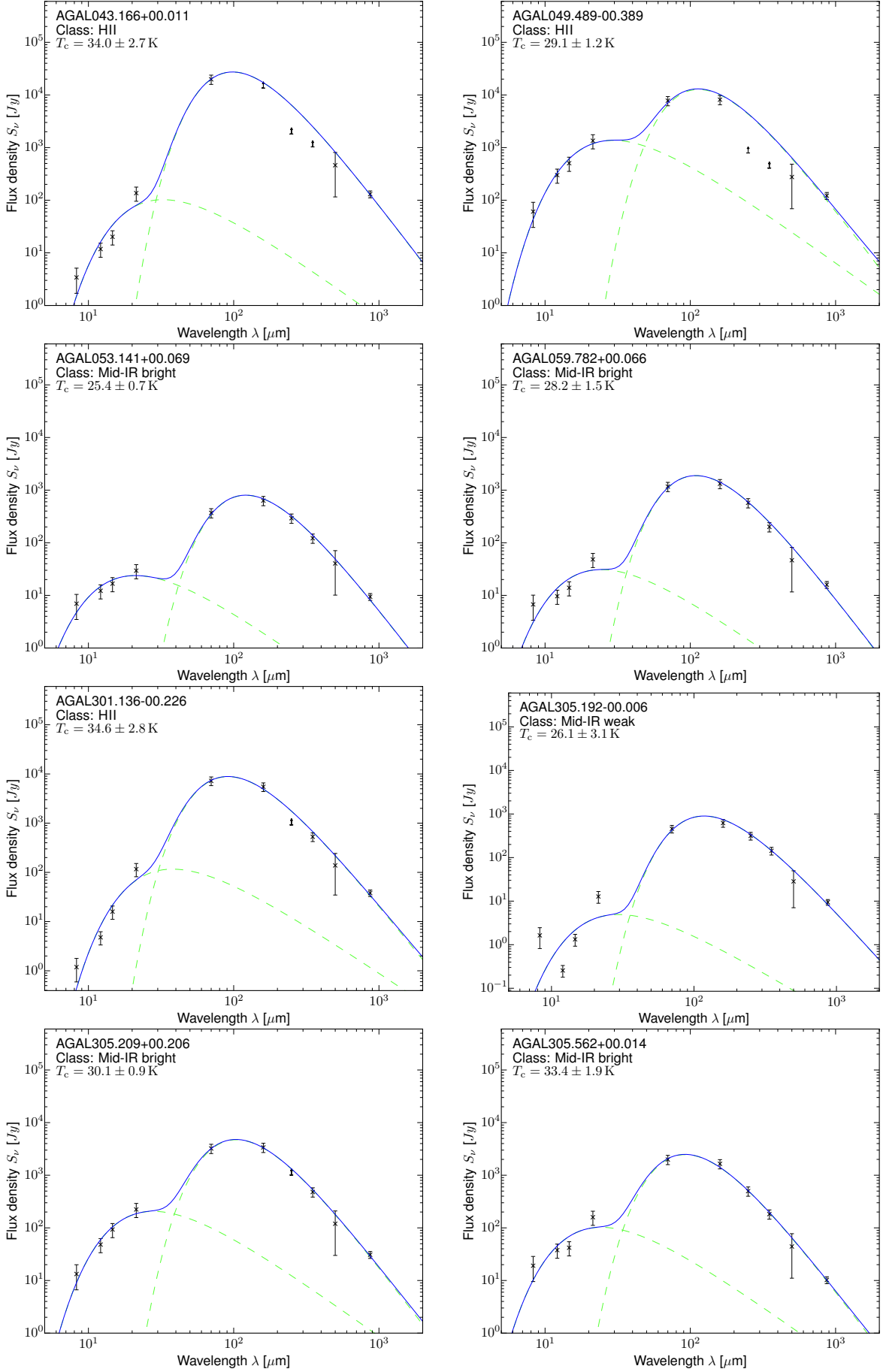
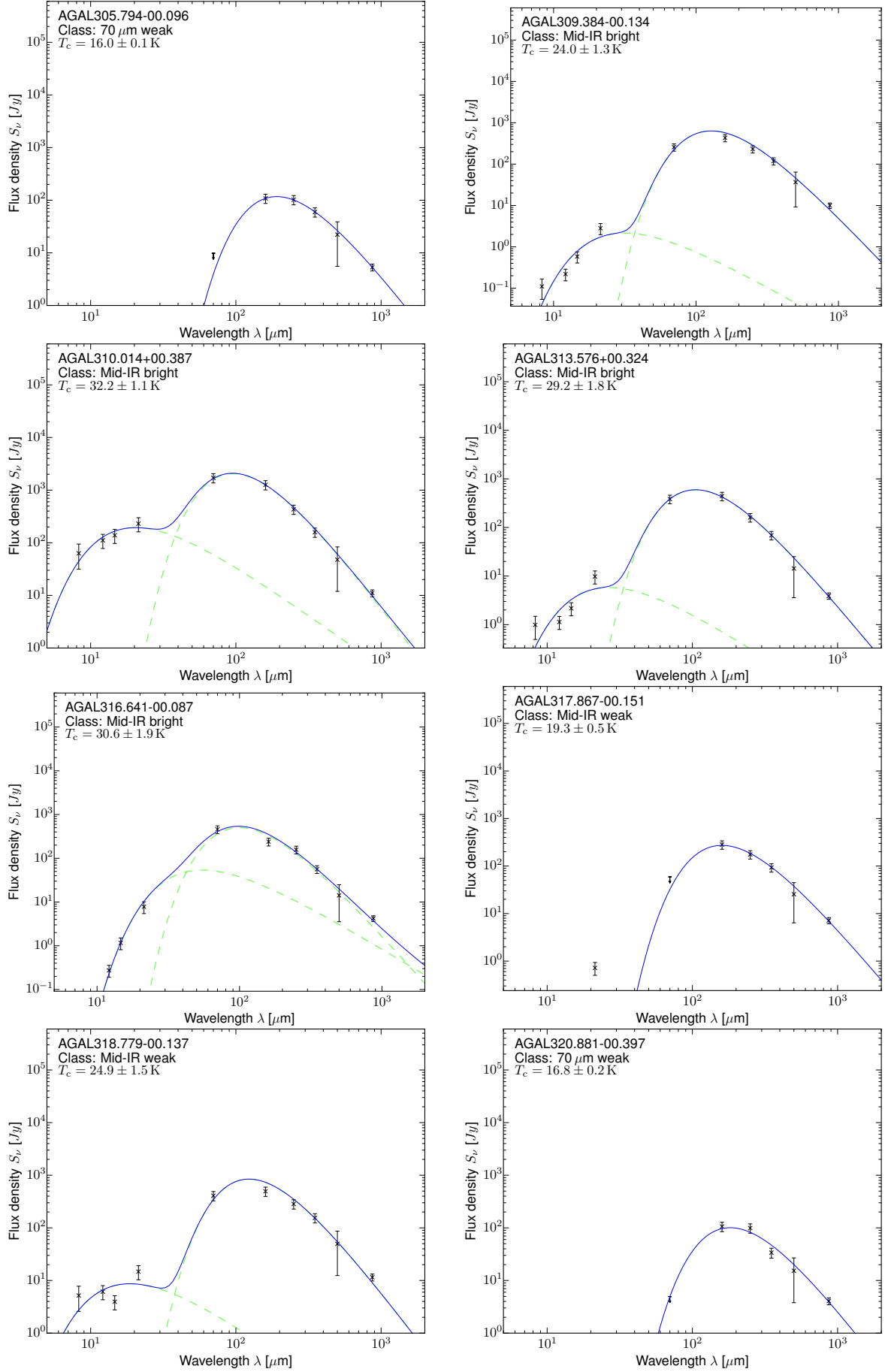


Fig. A.1. continued.

**Fig. A.1.** continued.

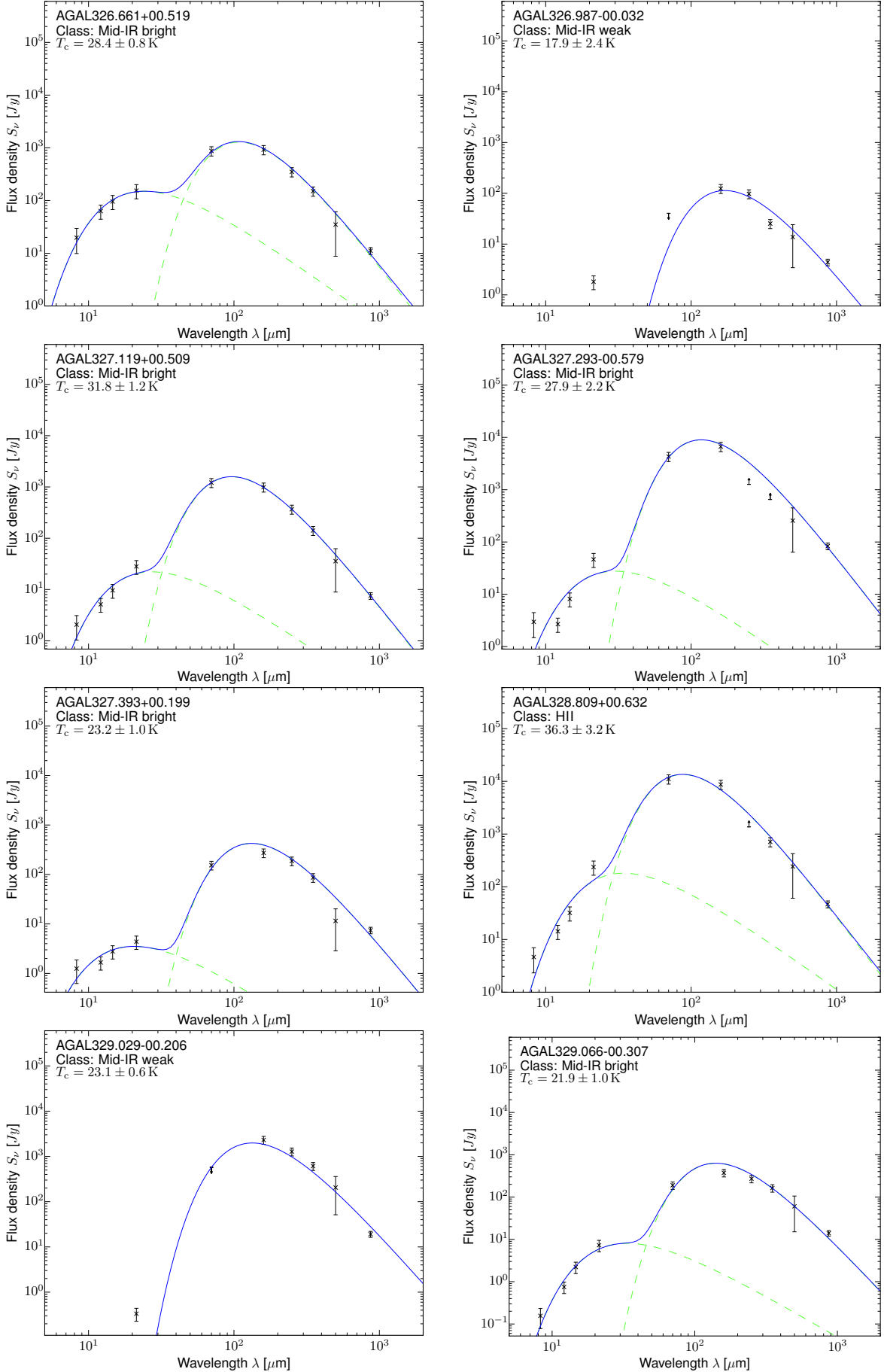
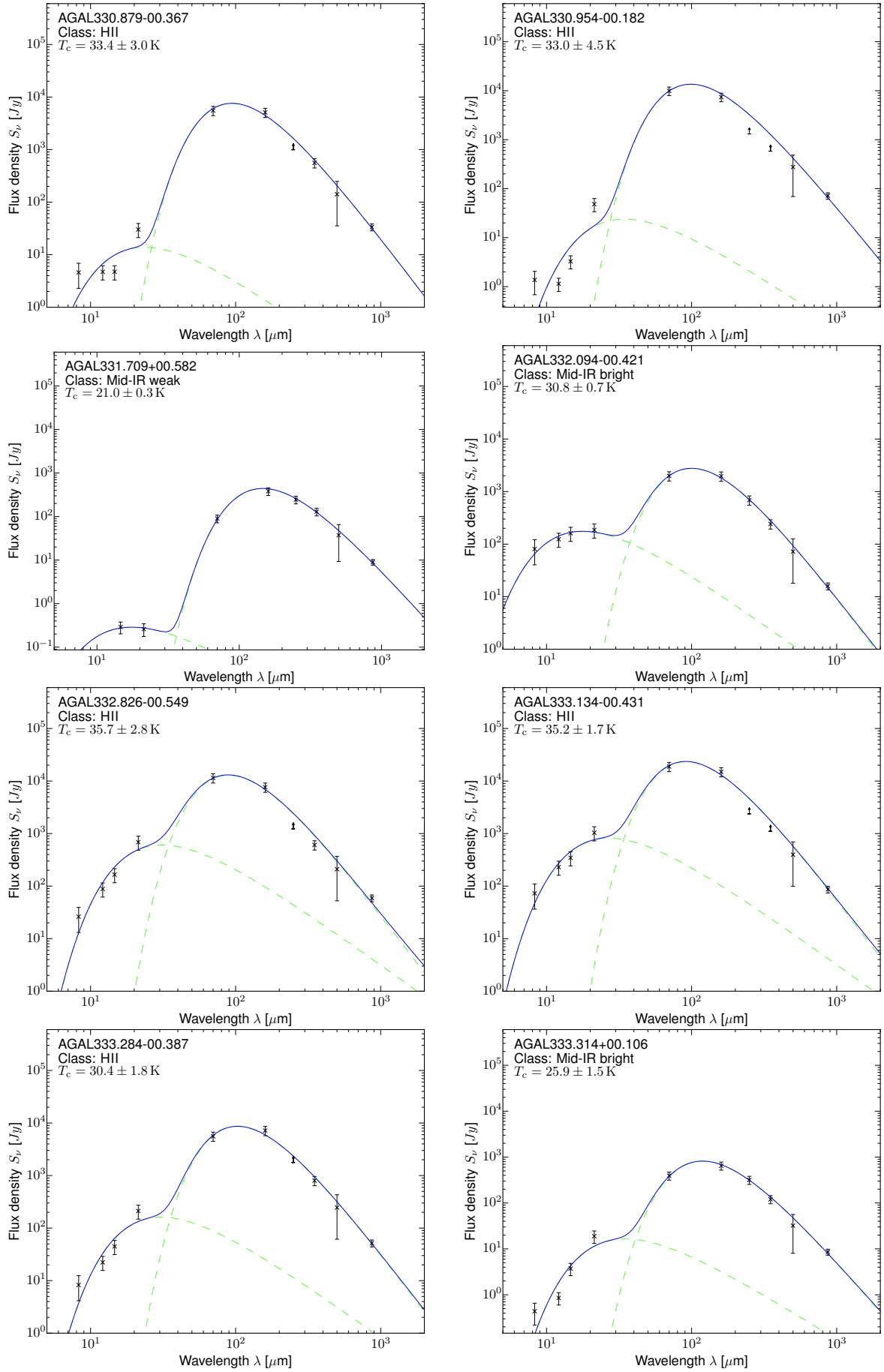


Fig. A.1. continued.

**Fig. A.1.** continued.

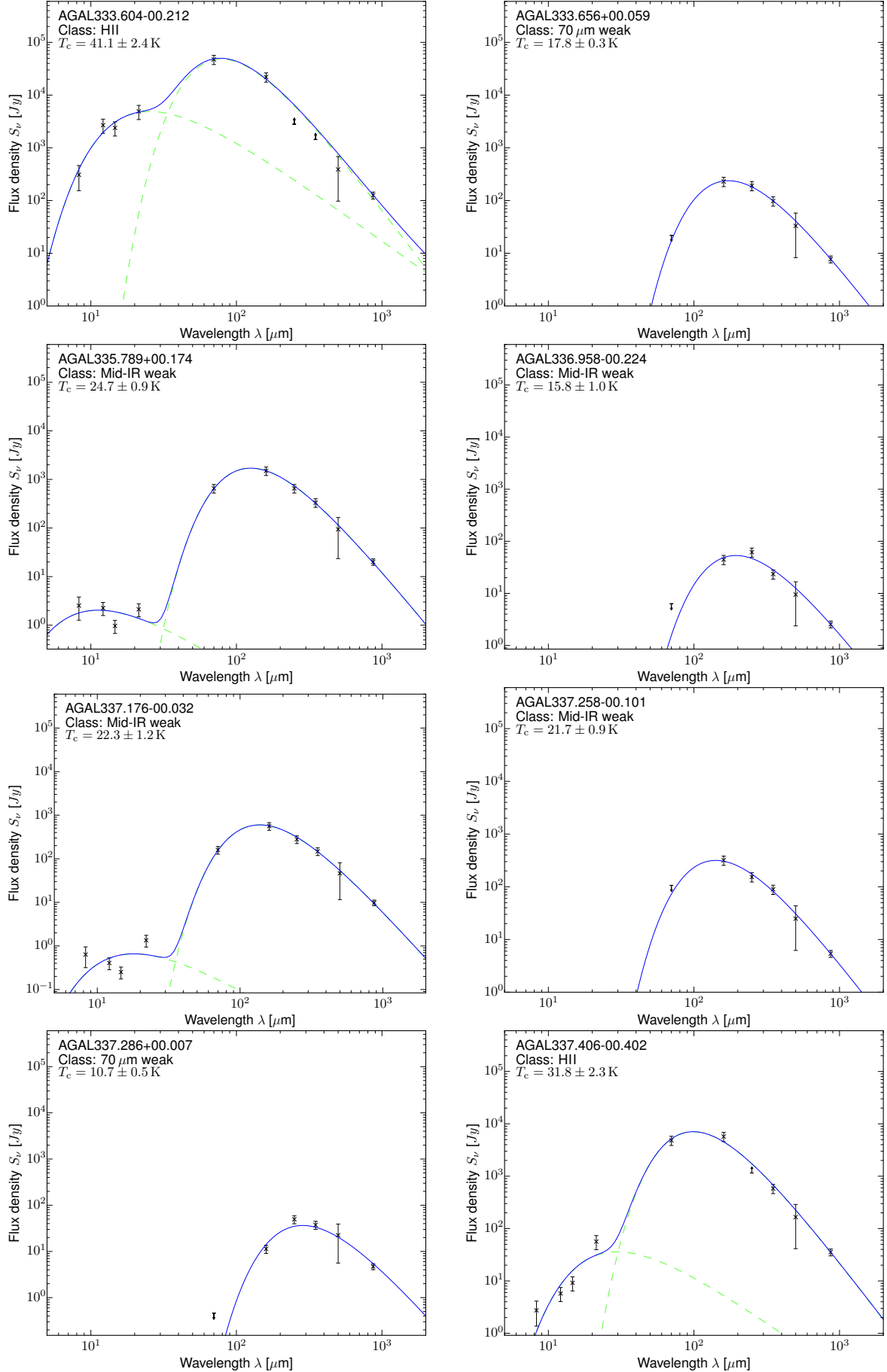
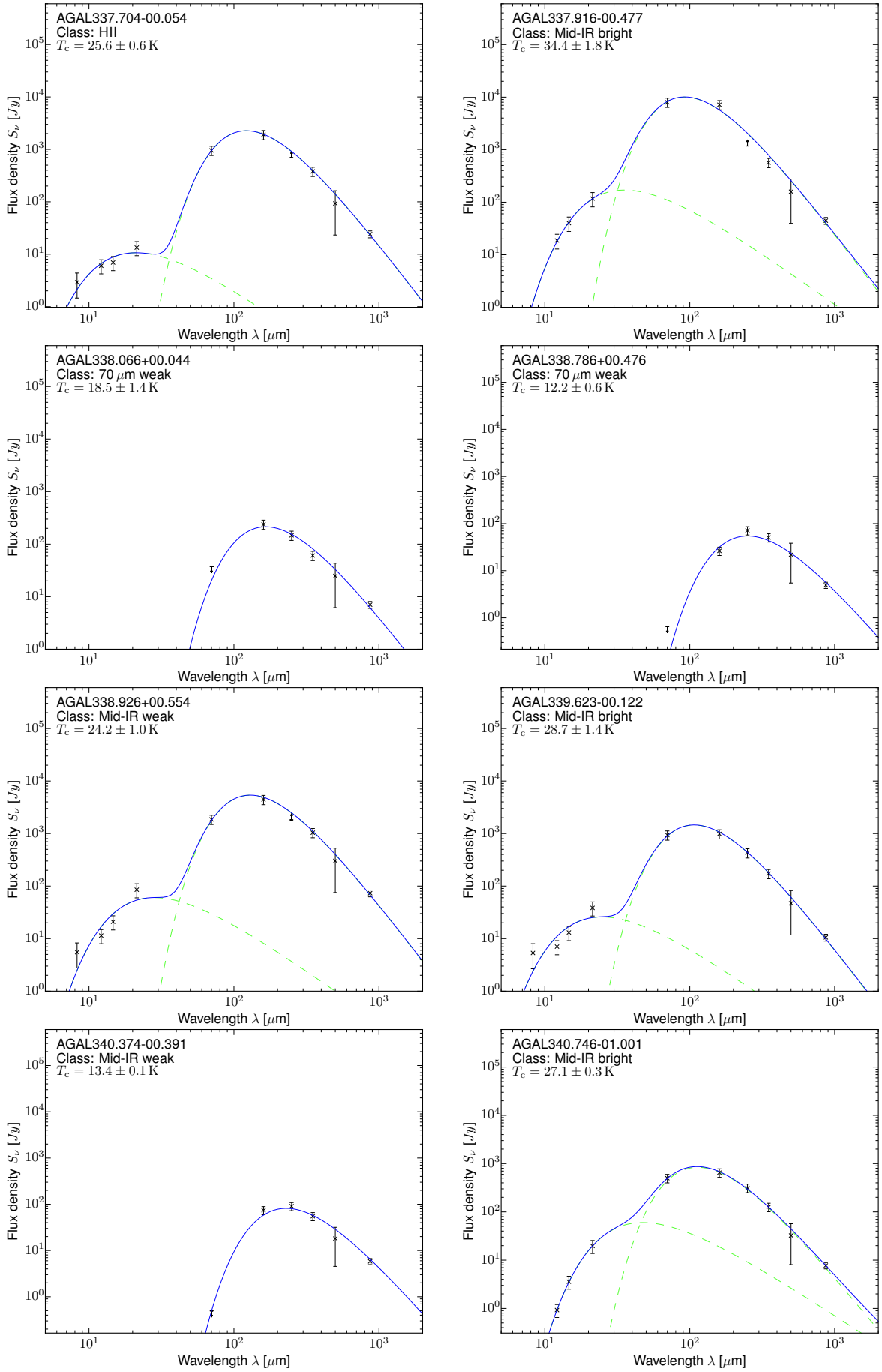


Fig. A.1. continued.

**Fig. A.1.** continued.

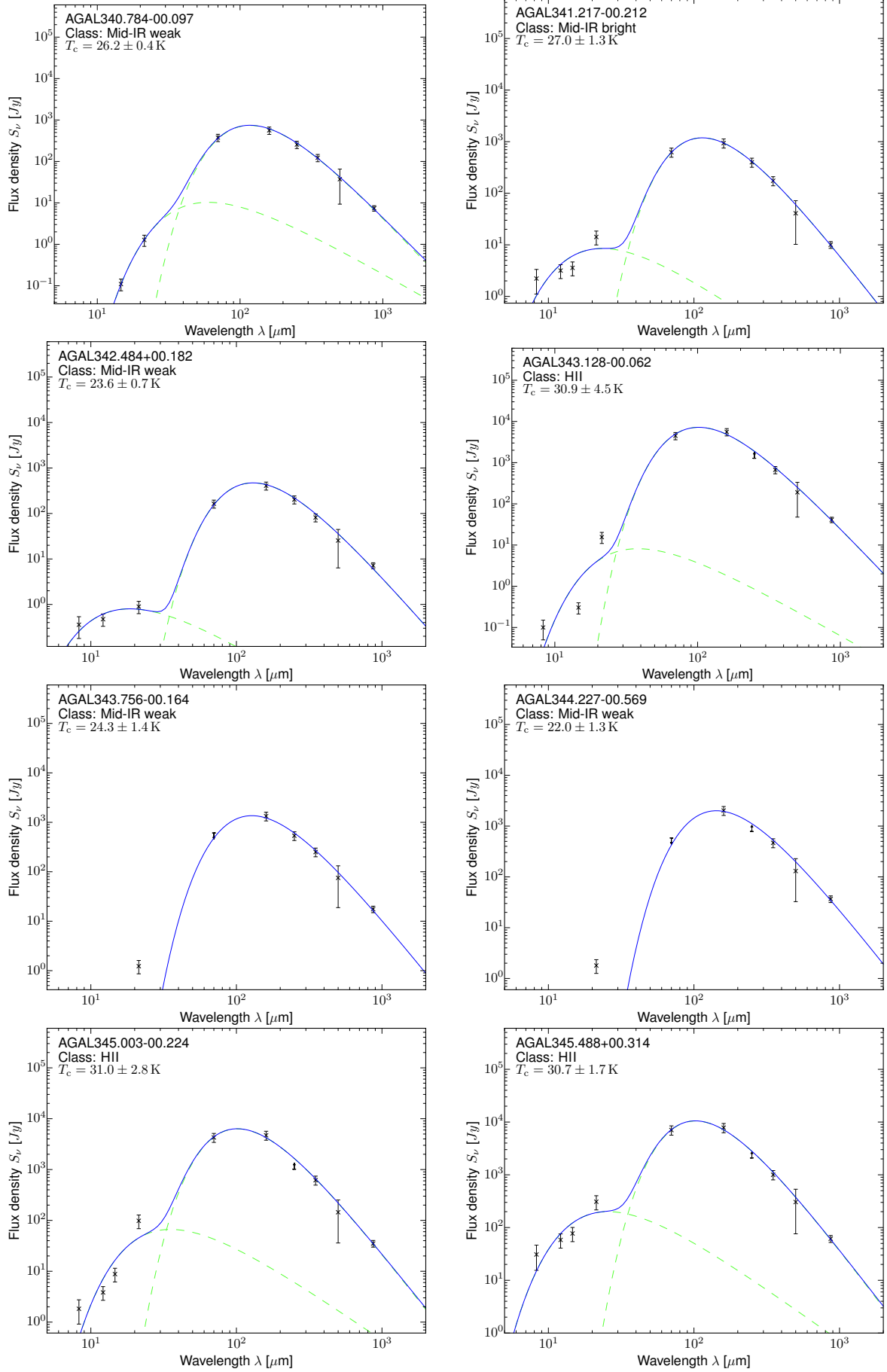
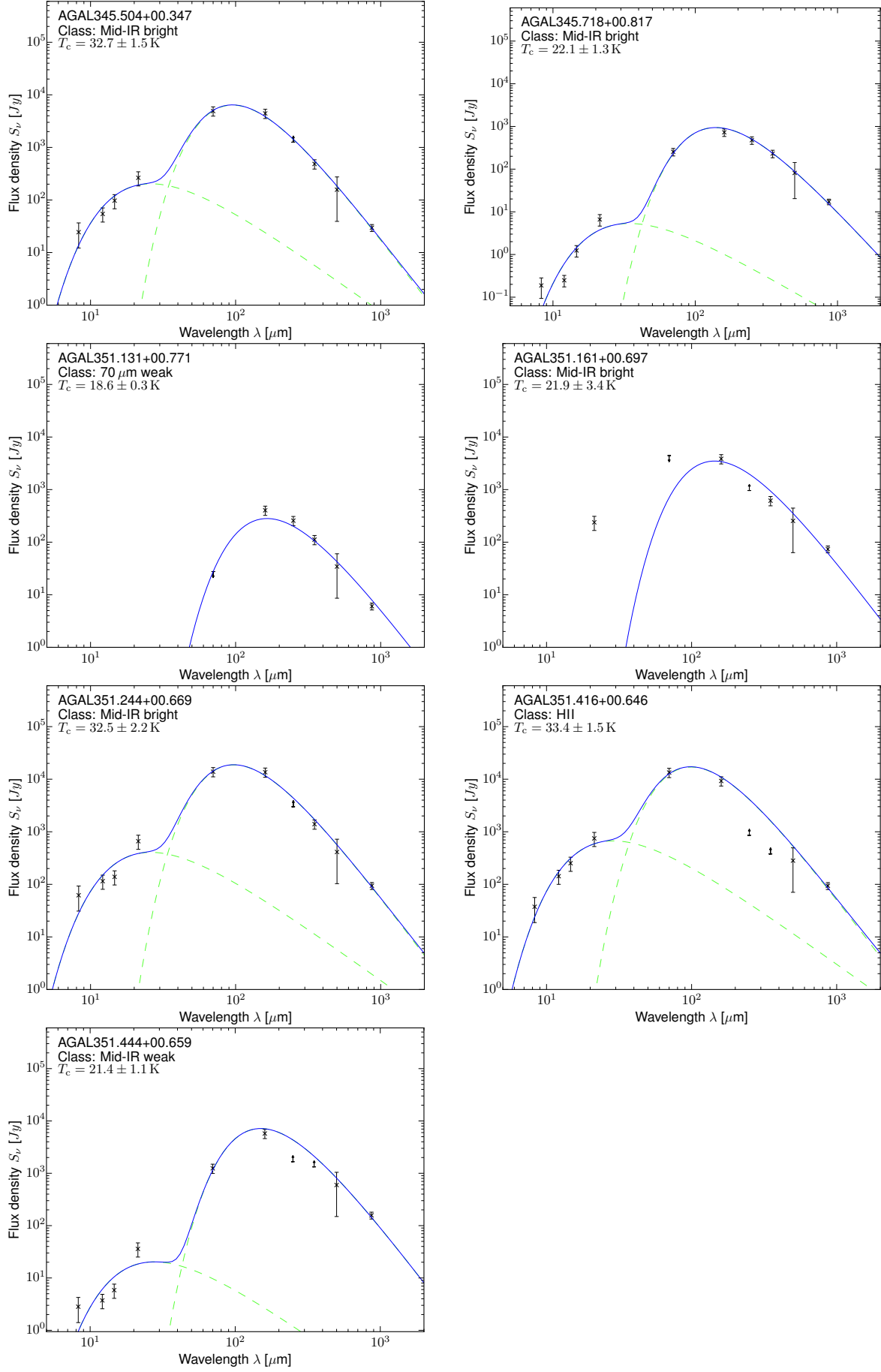


Fig. A.1. continued.

**Fig. A.1.** continued.

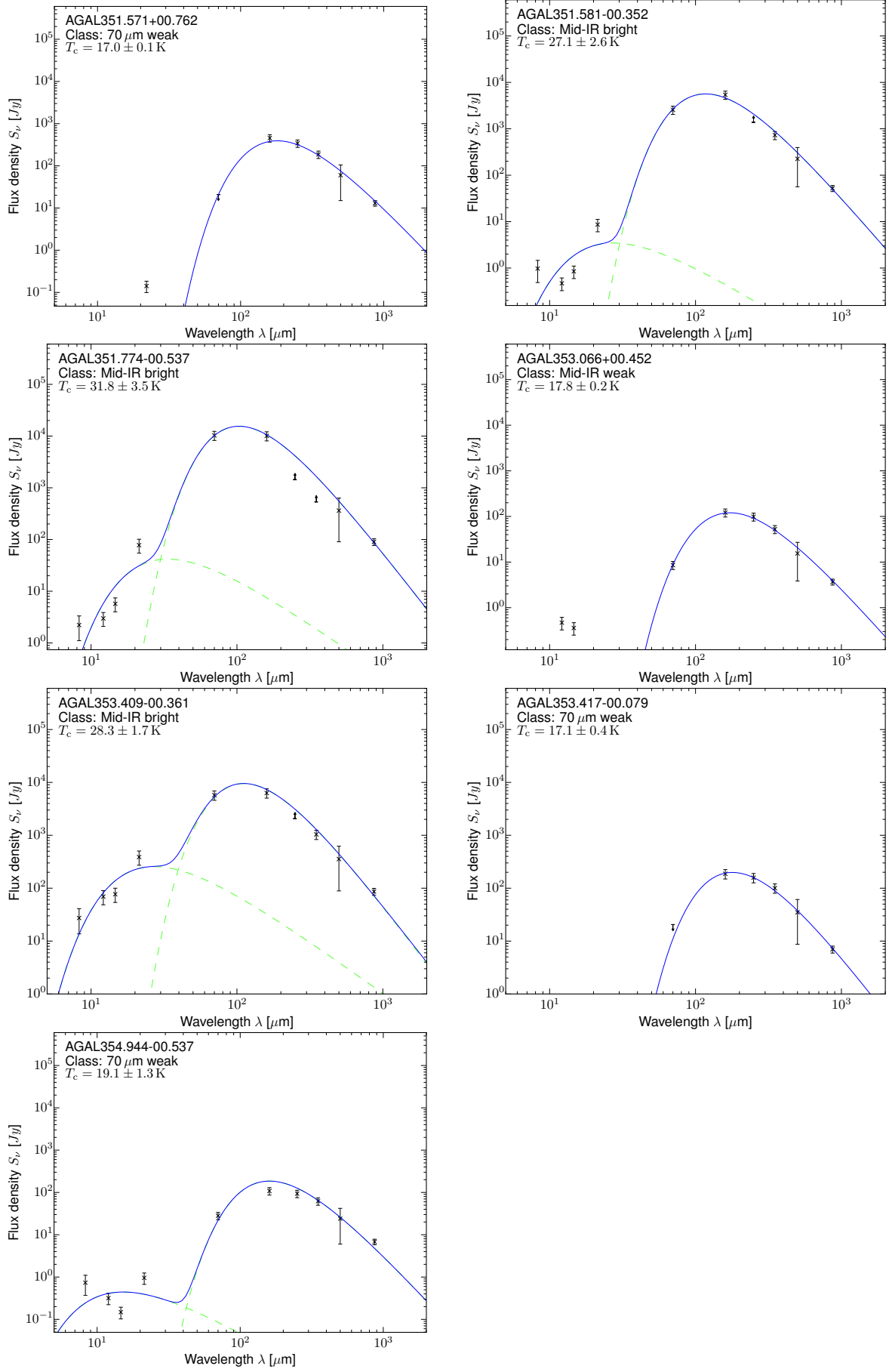


Fig. A.1. continued.